

BIOCHEMISTRY

Complexes of the neurotensin receptor 1 with small-molecule ligands reveal structural determinants of full, partial, and inverse agonism

Mattia Deluigi^{1*}, Alexander Klipp^{1*}, Christoph Klenk^{1*}, Lisa Merklinger^{1†}, Stefanie A. Eberle^{1‡}, Lena Morstein¹, Philipp Heine^{1§}, Peer R. E. Mittl¹, Patrick Ernst^{1||}, Theodore M. Kamenecka², Yuanjun He², Santiago Vacca¹, Pascal Egloff^{1#}, Annemarie Honegger¹, Andreas Plückthun^{1**}

Neurotensin receptor 1 (NTSR1) and related G protein–coupled receptors of the ghrelin family are clinically unexploited, and several mechanistic aspects of their activation and inactivation have remained unclear. Enabled by a new crystallization design, we present five new structures: apo-state NTSR1 as well as complexes with nonpeptide inverse agonists SR48692 and SR142948A, partial agonist RTI-3a, and the novel full agonist SRI-9829, providing structural rationales on how ligands modulate NTSR1. The inverse agonists favor a large extracellular opening of helices VI and VII, undescribed so far for NTSR1, causing a constriction of the intracellular portion. In contrast, the full and partial agonists induce a binding site contraction, and their efficacy correlates with the ability to mimic the binding mode of the endogenous agonist neurotensin. Providing evidence of helical and side-chain rearrangements modulating receptor activation, our structural and functional data expand the mechanistic understanding of NTSR1 and potentially other peptidergic receptors.

INTRODUCTION

The neurotensin receptor 1 (NTSR1) is a peptide-binding G protein–coupled receptor (GPCR) belonging to the ghrelin receptor family (1, 2), which encompasses several physiologically important receptors, yet all clinically unexploited to date (3, 4). NTSR1 exerts its function upon activation by the endogenous 13–amino acid peptide agonist neurotensin (NTS) and the NTS-related hexapeptide neuromedin N. The C-terminal hexapeptide portion of NTS, NTS_{8–13} (H-Arg₈-Arg₉-Pro₁₀-Tyr₁₁-Ile₁₂-Leu₁₃-OH; Fig. 1A), represents the binding epitope and contains all determinants for NTSR1 activation (5–7). Previously reported structures of NTSR1 (8–12) have elucidated the binding mode of NTS_{8–13} and provided insights into the mechanism of receptor activation. However, critically, the lack of structures in complex with antagonists or inverse agonists has precluded proper characterization of the inactive state, and thus, several mechanistic aspects of receptor activation and inactivation have remained unclear. Moreover, despite considerable efforts, the detailed structural rationales behind the mode of action of nonpeptide agonists and inverse agonists have largely remained unknown or hypothetical, as so far only the structure in complex with the peptide full agonist could be determined.

¹Department of Biochemistry, University of Zurich, Winterthurerstrasse 190, CH-8057 Zurich, Switzerland. ²Department of Molecular Medicine, The Scripps Research Institute, Scripps Florida, 130 Scripps Way #A2A, Jupiter, FL 33458, USA.

*These authors contributed equally to this work.

†Present address: Department of Biotechnology and Biomedicine, Technical University of Denmark, Søtofts Plads, 2800 Kgs. Lyngby, Denmark.

‡Present address: Department of Biomedical Sciences, Faculty of Health and Medical Sciences, University of Copenhagen, Blegdamsvej 3B, 2200 Copenhagen, Denmark.

§Present address: Takeda Pharma AG, Thurgauerstrasse 130, CH-8152 Glattpark, Switzerland.

||Present address: Faculty of Medicine, University of Zurich, Pestalozzistrasse 3/5, CH-8091, Zurich, Switzerland.

#Present address: Linkster Therapeutics AG, Stampfenbachstrasse 142, CH-8006 Zurich, Switzerland.

**Corresponding author. Email: plueckthun@bioc.uzh.ch

To elucidate structural determinants of full, partial, and inverse agonism, we had to find a way to obtain diffracting crystals of all of these states with small-molecule ligands. To accomplish this task, we established a new crystallization chaperone design by fusing a designed ankyrin repeat protein (DARPin) to NTSR1, thereby expanding the toolchest of fusion proteins that help GPCRs to crystallize. This strategy has now allowed us to solve the x-ray structures of NTSR1 in the apo state as well as in complex with small-molecule ligands (Fig. 1A), ranging from the inverse agonists SR48692 and SR142948A to the partial agonist RTI-3a and the novel full agonist SRI-9829, and to compare these to the NTSR1 structure bound to NTS_{8–13}.

The chemically related nonpeptide ligands SR48692 (Meclintertant) and SR142948A were identified by industry-led efforts over two decades ago (13, 14). These compounds competitively antagonize NTS-mediated effects, such as tumor promotion in various cancers (15–18). Furthermore, they were shown to reduce the level of basal activity in constitutively active NTSR1 mutants, revealing inverse agonist properties (19, 20). More recently, academic efforts aimed to discover nonpeptide agonists that are metabolically stable and orally available. Replacement of the adamantyl moiety of SR48692 with L-Leu resulted in “compound 3a” (21), a partial agonist developed at the Research Triangle Institute and thus named RTI-3a herein. Exploration of different chemical scaffolds led to the discovery of indole-based full agonists (22), and further work on this chemical series resulted in the development of SRI-9829, a novel nonpeptide full agonist that we disclose in this study (Fig. 1, A and E).

Despite these efforts and the many pathophysiological processes in which NTSR1 is involved, no drugs targeting this receptor have been clinically approved to date (3, 4). In the central nervous system, NTSR1 modulates several neuroendocrine and neurotransmitter systems, linking this receptor to psychostimulant addiction, schizophrenia, Parkinson’s disease, and other neurodegenerative diseases (23, 24). In the periphery, NTSR1 contributes to the regulation of the gastrointestinal and vascular systems (25, 26), implicating this receptor in intestinal inflammation (27), obesity and related metabolic

Copyright © 2021 The Authors, some rights reserved; exclusive licensee American Association for the Advancement of Science. No claim to original U.S. Government Works. Distributed under a Creative Commons Attribution NonCommercial License 4.0 (CC BY-NC).

Downloaded from <http://advances.sciencemag.org/> on January 29, 2021

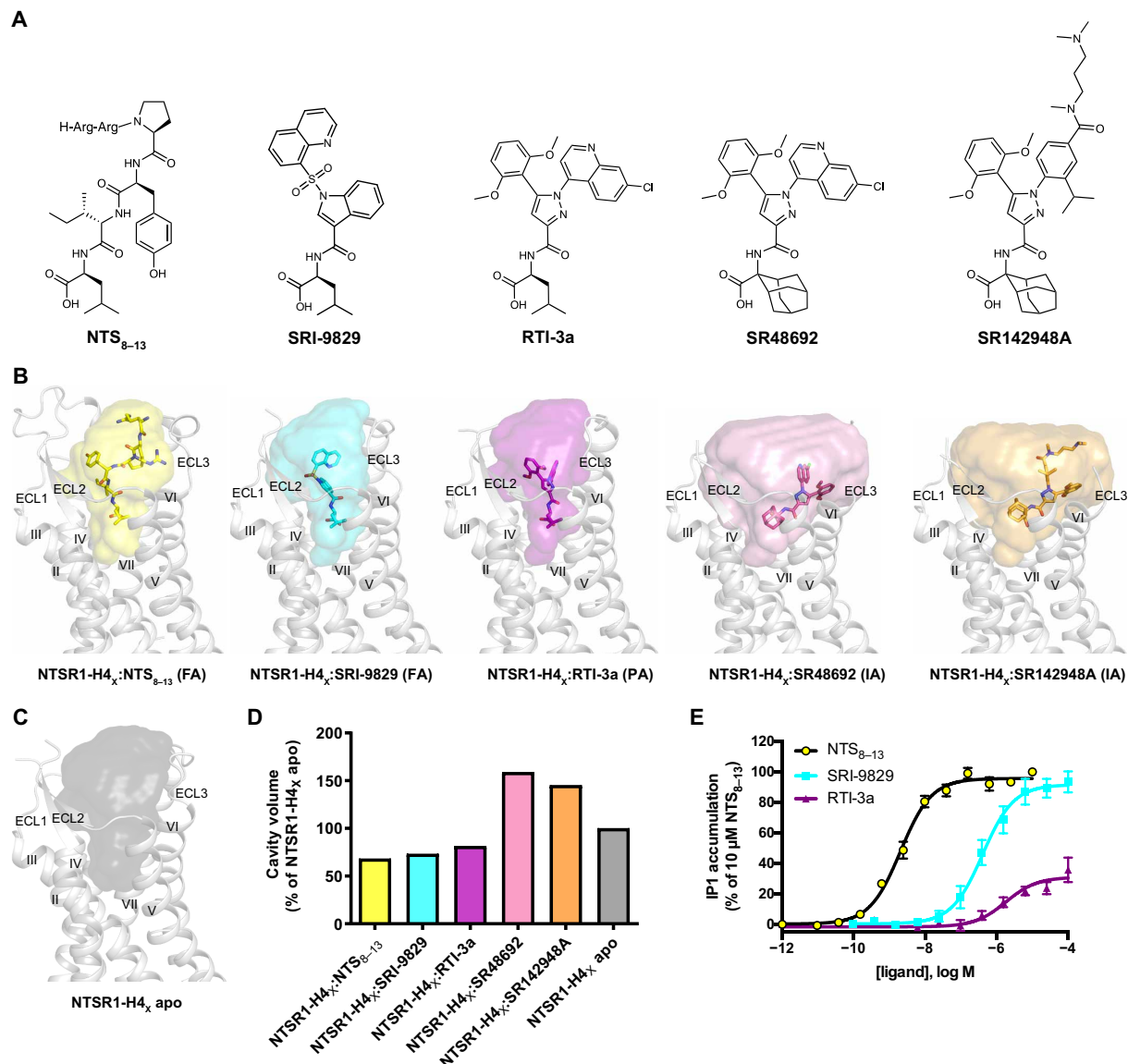


Fig. 1. Ligands induce a contraction or expansion of the orthosteric ligand-binding pocket depending on their pharmacological properties. (A) Chemical structures of full agonists NTS₈₋₁₃ and SRI-9829, partial agonist RTI-3a, and inverse agonists SR48692 and SR142948A. (B) Ligand-binding cavity volumes in the structures of NTSR1-H4_x in complex with the ligands indicated. FA, full agonist; PA, partial agonist; IA, inverse agonist; ECL, extracellular loop. (C) Corresponding cavity of apo-state NTSR1-H4_x. (D) Quantification of the ligand-binding cavity volumes relative to the apo state. The receptor backbone is depicted in cartoon representation in light gray. Ligands are shown as sticks, NTS₈₋₁₃ is colored yellow, SRI-9829 is colored cyan, RTI-3a is colored purple, SR48692 is colored pink, and SR142948A is colored orange. Oxygen, nitrogen, and chlorine atoms are depicted in red, blue, and green, respectively. The ligand-binding cavity volumes are shown as solid surfaces colored as the respective ligands and were calculated using the program POVME 2.0 (62). (E) Agonist-induced G_q signaling in cells expressing wild-type rNTSR1. Data were normalized to the response of 10 μM NTS₈₋₁₃ and are shown as means ± SEM from 3 to 11 independent experiments performed in duplicate. EC₅₀ (median effective concentration) values, NTS₈₋₁₃: 2.06 (1.62 to 2.61) nM; SRI-9829: 408.6 (262.9 to 635.1) nM; and RTI-3a: 1815 (789 to 4173) nM. E_{max} as % of 10 μM NTS₈₋₁₃, NTS₈₋₁₃: 95.7 (92.9 to 98.5); SRI-9829: 91.7 (84.7 to 98.6); and RTI-3a: 31.0 (25.6 to 36.4). The 95% confidence interval (CI) is given in parentheses.

disorders (28), and cardiovascular diseases (29, 30). NTS also acts as a growth factor on a variety of cells (31), and dysregulated NTSR1 signaling enhances proliferation, survival, and metastatic spreading of many cancers, correlating with a worse prognosis for patients (15–17).

The structures obtained in this study reveal the binding modes of ligands with diverse biological effects and the conformational changes induced by them. Notably, the inverse agonists adopt a tilt-

ed binding mode, which differs from previously published models (11, 32, 33). By widening a hydrophobic subpocket, the inverse agonists favor a large opening of the extracellular ends of transmembrane helix (TM) 6 and especially TM7, which has remained undescribed so far for NTSR1, translating in a closure of the G protein binding site. In contrast, the full and partial agonists act in the opposite direction, inducing a contraction of the binding site via a precise pattern of molecular contacts, and their efficacy correlates

with the ability to mimic the binding mode of the endogenous peptide agonist NTS. Last, the helical and side-chain rearrangements observed in the extracellular receptor half, in combination with functional data, provide detailed insights into the transmission of the activation trigger to the cytosolic side through a polar network and an aromatic cluster beneath the agonist pocket. As several crucial residues are conserved in related peptide-binding GPCRs, a better comprehension of NTSR1 mechanisms has the potential to improve our understanding of several other receptors, as well as how to convert peptide agonists into small-molecule full and inverse agonists. Furthermore, the structures presented here and our findings provide a solid basis for the optimization of ligands that could be useful in the treatment of cancers and neurological and metabolic disorders.

RESULTS

NTSR1 crystallization construct

Successful crystallization of NTSR1 previously relied on stabilized rat NTSR1 (rNTSR1) variants and the use of NTS₈₋₁₃ to further enhance stability and reduce conformational flexibility (8–11). Attempts to obtain crystals of the apo state or of complexes with small-molecule ligands failed, however, probably due to the lack of sufficient conformational stabilization and the inability to establish crystal contacts. To overcome these obstacles, we took advantage of a previously developed and highly stable rNTSR1 mutant, NTSR1-H4 (table S1) (34, 35). Previous studies with NTSR1-H4 enabled identification of new ligands that show agonistic or antagonistic properties on the wild-type receptor (36, 37). Compared to wild-type rNTSR1, NTSR1-H4 displays higher affinity for full agonists but decreased affinity for inverse agonists (fig. S1 and table S2), suggesting conformational stabilization. This property is likely a key for successful cocrystallization of agonistic compounds that show low affinity to the wild-type receptor or weak efficacy (partial agonists); however, importantly, NTSR1-H4 also retained the ability to undergo agonist-induced and inverse agonist-induced conformational changes, as described below.

As none of the initially investigated constructs crystallized, neither when fused to commonly used crystallization chaperones (38) nor without any fusion, we designed a new fusion construct. We fused the C-terminal end of TM7 of NTSR1-H4 to the DARPin D12 crystallization chaperone (39–41) via a shared helix (fig. S2). This construct, referred to as NTSR1-H4_X, readily crystallized in complex with the full agonists NTS₈₋₁₃ and SRI-9829, the partial agonist RTI-3a, the inverse agonists SR48692 and SR142948A, as well as in the apo state (figs. S3, A to F, and S4).

The resolution of the structures ranged from 2.5 to 3.2 Å (table S3), and the good quality of the electron density allowed unambiguous modeling of the ligands and key receptor residues discussed herein (figs. S5 and S6). The presence of the fused DARPin neither perturbed ligand affinities (fig. S1 and table S2), nor was there any relevant structural deviation in the seven transmembrane (7TM) bundle compared to the same receptor mutant crystallized without DARPin [Protein Data Bank (PDB) ID: 4BWB] (9) (fig. S7). In addition, no relevant deviation was observed in the NTS binding site of NTSR1-H4_X compared to the structure of a minimal mutant with retained signaling properties, NTSR1-ELF (PDB ID: 4XEE) (10) (fig. S8, A and B).

Architecture of agonist-induced and inverse agonist-bound complexes and of apo structure

Comparison of the apo structure with the agonistic and inverse agonistic ligand complexes revealed notable differences in the volume

of the orthosteric ligand-binding cavities; while the agonists induced a reduction of the accessible volume, the inverse agonists acted in the opposite direction, leading to a marked expansion of the orthosteric cavity (Fig. 1, B to D).

The contraction of the orthosteric pocket of NTSR1-H4_X bound to NTS₈₋₁₃ is comparable to what has been observed in the active-state hNTSR1-G_{i1} complex (PDB ID: 6OS9) (12) (fig. S8C). The complex of NTSR1-H4_X with the nonpeptide full agonist SRI-9829 adopts a highly similar conformation, with the extracellular tip of TM7 even slightly more contracted toward the receptor center (Fig. 2A and fig. S8D). At the extracellular side, both agonist-bound complexes thus resemble the fully active state; however, in the absence of a G protein, TM6 occludes the G protein-binding cavity (fig. S9), reflecting stabilization in a signaling-inactive conformation at the cytosolic side (42).

The complex with the partial agonist RTI-3a exhibits a similar arrangement of the helical bundle as observed with the full agonists (Fig. 2B). However, a subtle difference in the position of the extracellular tip of TM7—more distant from the receptor center—and rearrangements of key side chains in the orthosteric binding site (described below) may suggest why the partial agonist is less effective than the full agonists in inducing and stabilizing a contracted ligand-binding pocket.

This trend is confirmed in the apo-state structure, which appears to adopt an intermediate state at the extracellular side according to the binding site volume (Fig. 1D). In particular, the extracellular tip of TM7 appears to be more distant from the receptor center compared to the NTS₈₋₁₃ complex (by 2.0 Å) (Fig. 2B) and the SRI-9829 complex (by 3.7 Å), as measured between corresponding C α atoms of residue 342^{7,26} (superscripts indicate Ballesteros-Weinstein numbering).

Notably, the complexes of NTSR1-H4_X with the inverse agonists SR48692 and SR142948A exhibit a wider binding site (Fig. 1, B and D), mainly as a consequence of TM6 and TM7 adopting a more outward-pointing orientation at the extracellular side compared to the NTS₈₋₁₃ complex (by 3.0 and 4.9 Å, respectively) (Fig. 2C). As a structural consequence, TM6 adopts a more closed conformation at the intracellular side, completely occluding the G protein-binding cavity (fig. S10A). Our data thus corroborate the notion that a less contracted binding site is characteristic of the inactive state of class A GPCRs (43, 44) and reveal that, in this peptidergic GPCR, TM6 and especially TM7 provide the main lever arms, which could thus apply as well to closely related receptors.

The high-resolution structures we obtained in the active- and inactive-like states enabled us to analyze the determinants of NTSR1 activation and inactivation in great detail. However, we anticipated that four mutations of NTSR1-H4_X, i.e., E124^{2,61}D, D150^{3,33}E, F358^{7,42}V, and S362^{7,46}A, may limit the extent of this analysis. E124^{2,61} and D150^{3,33} are part of a polar network below the NTS₈₋₁₃ binding site that has been proposed to link agonist binding to the hydrophobic receptor core (10, 11, 45). The latter includes F358^{7,42}, while S362^{7,46} is part of the Na⁺-binding pocket. Therefore, we back-mutated (denoted “bm”) these four positions to wild-type residues, generating NTSR1-H4bm_X. Initial crystal hits of NTSR1-H4bm_X grew in far fewer conditions and to a smaller size than NTSR1-H4_X, presumably reflecting a loss of conformational stability. Nevertheless, we were able to solve crystal structures in complex with NTS₈₋₁₃ and SR48692 at 2.6- and 2.7-Å resolution, respectively (figs. S3, G and H, S11, and fig. S12 and table S4). Similarly to NTSR1-H4_X, the complex of NTSR1-H4bm_X with SR48692 exhibits a very similar inactive-like

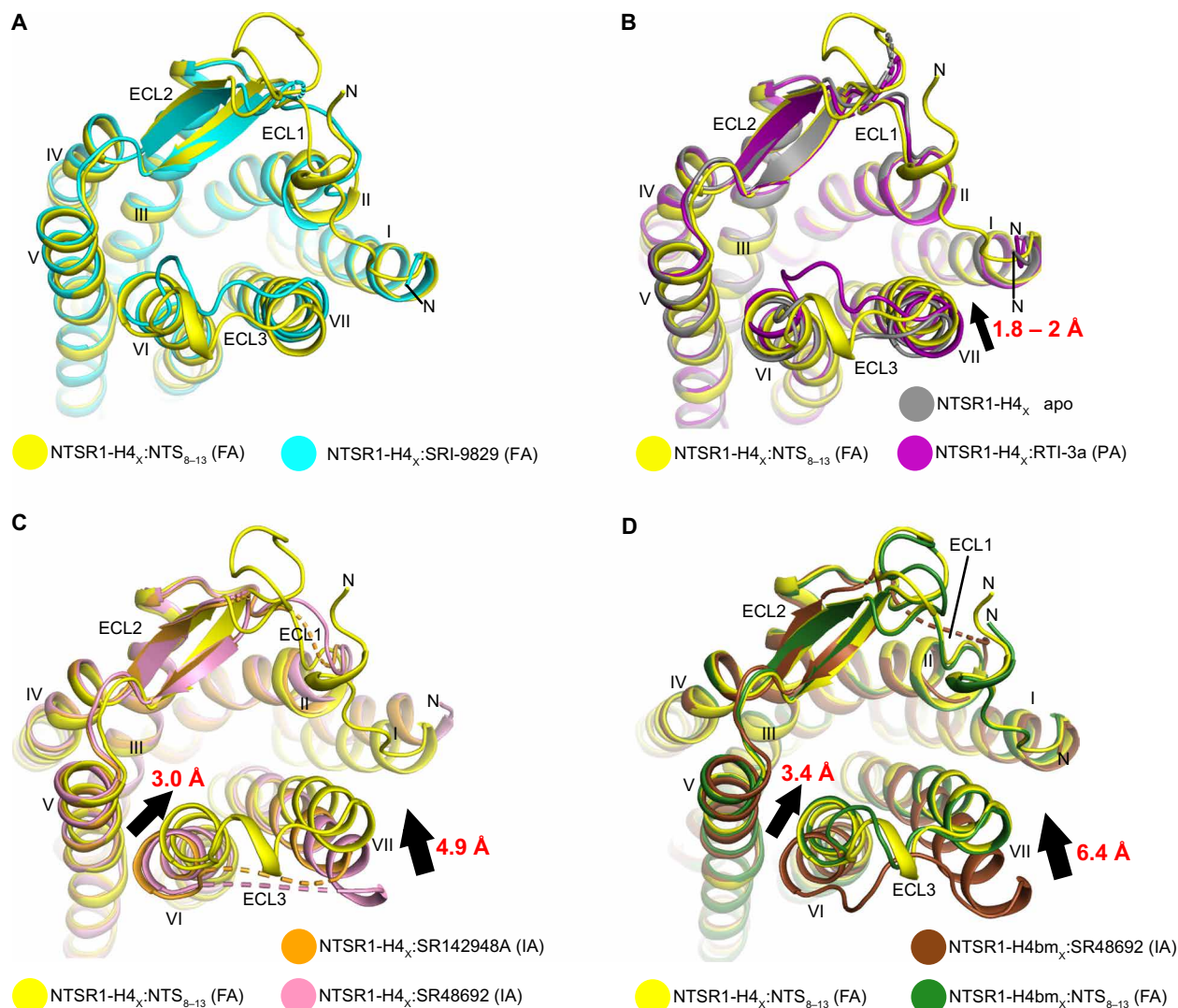


Fig. 2. Architecture of rNTSR1 structures with full agonist (FA), partial agonist (PA), inverse agonist (IA), or in the apo state, all viewed from the extracellular side. For clarity, the ligands and the DARPIn fusion are omitted in these overview structures. (A) Overlay of the highly similar structures of NTSR1-H4_x bound to the full agonists NTS₈₋₁₃ and SRI-9829. (B) Movement from apo state to partial to full agonist, as seen in NTSR1-H4_x: apo state, RTI-3a (PA), NTS₈₋₁₃ (FA). (C) Movement from inverse to full agonist, as seen in NTSR1-H4_x: SR48692 (IA), SR142948A (IA), NTS₈₋₁₃ (FA). (D) Movement from inverse to full agonist, as seen in the back-mutated NTSR1-H4bm_x construct; SR48692 (IA), NTS₈₋₁₃ (FA). The receptor backbone is depicted in cartoon representation and is colored as indicated in the legend. Shifts of the extracellular tips of TM6 and TM7 toward a more contracted binding site are indicated by black straight arrows. The helix tip movements in Å are indicated in red.

arrangement of the TMs (Fig. 2D) [root mean square deviation for Ca atoms (RMSD_{Ca}) = 1.0 Å between SR48692-bound NTSR1-H4_x and NTSR1-H4bm_x], whereas the NTS₈₋₁₃-bound structure once again exhibits a fully contracted extracellular portion, emphasizing the ability of the agonist, but not of the inverse agonist, to trigger and stabilize the contraction of the binding site (by 3.4 Å at TM6 and 6.4 Å at TM7 toward the central axis, as seen in NTSR1-H4bm_x). Crucially, the aforementioned conformational changes in the extracellular portion are ligand-induced and do not depend on the crystallization method [vapor diffusion or lipidic cubic phase (LCP)], crystal packing, or the orientation of the DARPIn fusion (fig. S13). Although we do not draw conclusions regarding TM1, we observe a more outward-pointing arrangement in inverse agonist-bound NTSR1-H4_x compared to NTSR1-H4bm_x (Fig. 2, C and D) that might, however, be related to its intrinsic flexibility and to crystal packing forces.

Binding mode of the nonpeptide agonists

NTS₈₋₁₃ and the nonpeptide agonists SRI-9829 and RTI-3a largely share the same binding site (Fig. 3, A to C) (agonist-receptor interactions are listed in tables S5 to S7). The binding modes and contacts of the full agonist SRI-9829 and of the partial agonist RTI-3a overlap to different extents with those of NTS₈₋₁₃ (Fig. 3, A to C and E and F), suggesting that this may underlie their different pharmacological properties.

In the lower part of the binding site, the L-Leu moieties of all three agonists form highly similar contacts with the receptor. The carboxylate of the L-Leu moiety anchors the ligands to the binding site by forming a salt bridge with R327^{6,54} and a strong hydrogen bond with Y146^{3,29}, while the isobutyl chain targets a hydrophobic subpocket, establishing extensive van der Waals interactions with residues of TM3 to TM6 and extracellular loop 2 (ECL2) (Y146^{3,29},

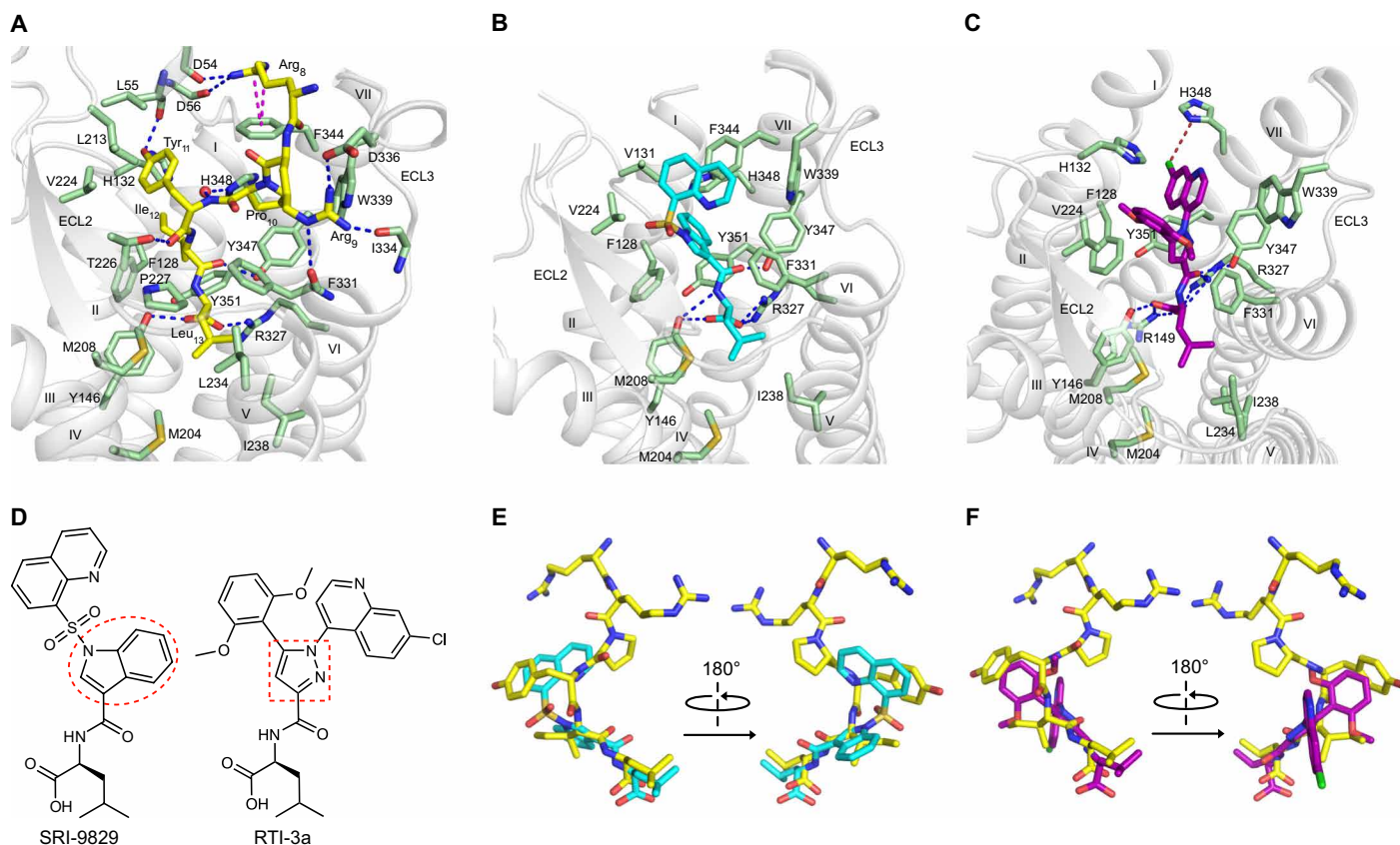


Fig. 3. Agonist-binding pockets of rNTSR1 and superposition of agonist-binding modes. (A to C) Detailed interactions of (A) NTS₈₋₁₃ (FA), (B) SRI-9829 (FA), and (C) RTI-3a (PA) with the receptor, viewed from the extracellular side. FA, full agonist; PA, partial agonist. The receptor backbone is depicted in cartoon representation and is colored in light gray. Ligands are shown as sticks; colors are as in Fig. 1. Interacting receptor residues are shown as sticks in pale green. L213 and L234 are mutations present in NTS₈₋₁₃-H4 (R and V in wild-type rNTSR1, respectively). An ordered water molecule involved in NTS₈₋₁₃ binding is shown as a red sphere. H-bonds and salt bridges are depicted by dashed blue lines, cation- π interactions are depicted by dashed magenta lines, and halogen- π interactions are depicted by dashed red lines. The DARPIn fusion has been omitted for clarity. (D) Chemical structures of SRI-9829 and RTI-3a. The core scaffold of each ligand is highlighted either by a dashed red circle (indole group) or by a dashed red rectangle (pyrazole group). (E and F) Comparison of the binding modes of (E) NTS₈₋₁₃ and SRI-9829 (both FA) and of (F) NTS₈₋₁₃ (FA) and RTI-3a (PA). After superposition of the complexes, the receptor has been omitted for clarity.

M204^{4.60}, M208^{4.64}, P227^{ECL2}, I238^{5.39}, and F331^{6.58}). The importance of these contacts is underscored by the observation that L-Leu is highly preferred in terms of binding and agonist activity over its enantiomer D-Leu as well as many other terminal amino acids (21, 22, 46). In all three agonists, the L-Leu moiety is connected with an amide group to the rest of the ligand (Fig. 1A), and the corresponding amide oxygen is engaged in a strong hydrogen bond with TM7 (Y347^{7.31}).

SRI-9829 and RTI-3a considerably differ in their chemical core scaffolds (Fig. 3D). The indole core of SRI-9829 occupies a similar space as the backbone and side chain of Ile₁₂ in the NTS₈₋₁₃ complex (Fig. 3E), and it interacts with the numerous surrounding aromatic residues (F128^{2.65}, F331^{6.58}, F344^{7.28}, Y347^{7.31}, H348^{7.32}, and Y351^{7.35}) (Fig. 3B). In strong contrast, the pyrazole core of RTI-3a occupies a substantially different space than Ile₁₂ in the NTS₈₋₁₃ complex (Fig. 3F), and it interacts with fewer aromatic residues (F128^{2.65}, F331^{6.58}, Y347^{7.31}, and Y351^{7.35}) (Fig. 3C). In addition, SRI-9829 and RTI-3a also substantially differ in the contacts mediated by their substituents pointing toward the extracellular part of the pocket. In SRI-9829, the sulfonyl group points toward T226^{ECL2}, and the quinoline ring adopts a virtually ideal position to form aromatic

stacking with F344^{7.28} and an edge-to-face aromatic interaction with W339^{ECL3}, complemented by van der Waals contacts with V224^{ECL2} (Fig. 3B). The quinoline ring of SRI-9829 thus fills a similar space as between Tyr₁₁ and Pro₁₀ in the NTS₈₋₁₃ complex (Fig. 3E). Overall, the L-shaped binding mode of SRI-9829 is thus remarkably similar to that of the C-terminal tetrapeptide Pro₁₀-Tyr₁₁-Ile₁₂-Leu₁₃ of NTS₈₋₁₃. In light of the crucial role of this tetrapeptide portion in binding and agonist activity (5, 46, 47), the ability of the chemical groups of SRI-9829 to mimic its spatial arrangement and interactions is likely reflected in the full agonist properties of SRI-9829 at NTS₈₋₁₃.

In contrast to SRI-9829, the dimethoxyphenyl and chloroquinoline substituents of RTI-3a occupy a largely different space than Tyr₁₁ and Pro₁₀ in the NTS₈₋₁₃ complex (Fig. 3F). The dimethoxyphenyl moiety points toward Tyr₁₁ of the NTS₈₋₁₃ complex; however, its phenyl ring adopts a completely different orientation (Fig. 3, C and F). In addition, the chloroquinoline moiety occupies a subpocket that is entirely neglected in the NTS₈₋₁₃ and SRI-9829 complexes. While the aromatic ring system interacts with the surrounding residues (F128^{2.65}, W339^{ECL3}, F344^{7.28}, Y347^{7.31}, and Y351^{7.35}), the chlorine substituent points toward H348^{7.32} (Fig. 3C). Overall, although the

presence of the L-Leu moiety in RTI-3a fulfills an important prerequisite for NTSR1 agonists (21, 22, 46, 48), the large differences in the other parts of the ligand compared to NTS₈₋₁₃ and their structural consequences (see below) probably account for the reduced ability of RTI-3a to activate NTSR1.

The inverse agonists hinder contraction of the extracellular portion

In contrast to the agonists, the inverse agonists SR48692 and SR142948A are located in a wider binding pocket (Figs. 1B and 4, A to C, and fig. S14) and occupy mostly a different space than NTS₈₋₁₃ (Fig. 4, D and E); however, they share the same binding site as the peptide agonist. This is consistent with the previously reported finding that SR142948A binds entirely in the same site as NTS₈₋₁₃, as evidenced by chemical cross-linking experiments (20). Furthermore, their binding mode is in agreement with site-directed mutagenesis studies (note S1) and molecular dynamics simulations (20). The carboxylate group of both inverse agonists anchors to R327^{6,54}, similarly to the agonists; however, it hydrogen-bonds to Y351^{7,35} instead of Y146^{3,29}. Consistent with its nonpolar nature, the adamantyl moiety of both inverse agonists targets the same hydrophobic sub-

pocket as the L-Leu side chain of the agonists, forming contacts with residues of TM3 to TM6 and ECL2 (tables S10 and S11). Notably, the sole replacement of the adamantyl moiety of SR48692 with an L-Leu side chain converts this inverse agonist into the partial agonist RTI-3a (21), raising the question of which mechanisms underlie ligand-mediated receptor activation and inactivation.

On the basis of our crystal structures, it appears that inverse agonism is related to a steric effect exerted by the bulky adamantyl moiety. In contrast to the isobutyl chain of L-Leu, the adamantyl moiety favors a substantial widening of the hydrophobic subpocket at F331^{6,58} (Fig. 5 and fig. S15), thereby hindering the contraction of the extracellular receptor portion, which is observed for the agonists. Conversely, the shape of the isobutyl chain appears to be optimally tailored to induce and stabilize a contracted arrangement of TM6 at its extracellular tip. Following the widening of the hydrophobic subpocket favored by the adamantyl moiety, the remaining chemical groups of both inverse agonists adopt a similar binding mode (Fig. 4F), substantially further away from the receptor center than NTS₈₋₁₃ (Fig. 4, D and E). As a consequence and in strong contrast to the agonists, the interactions with activation-crucial residues in ECL3 and TM7 (outlined below) are absent or weak, and there are

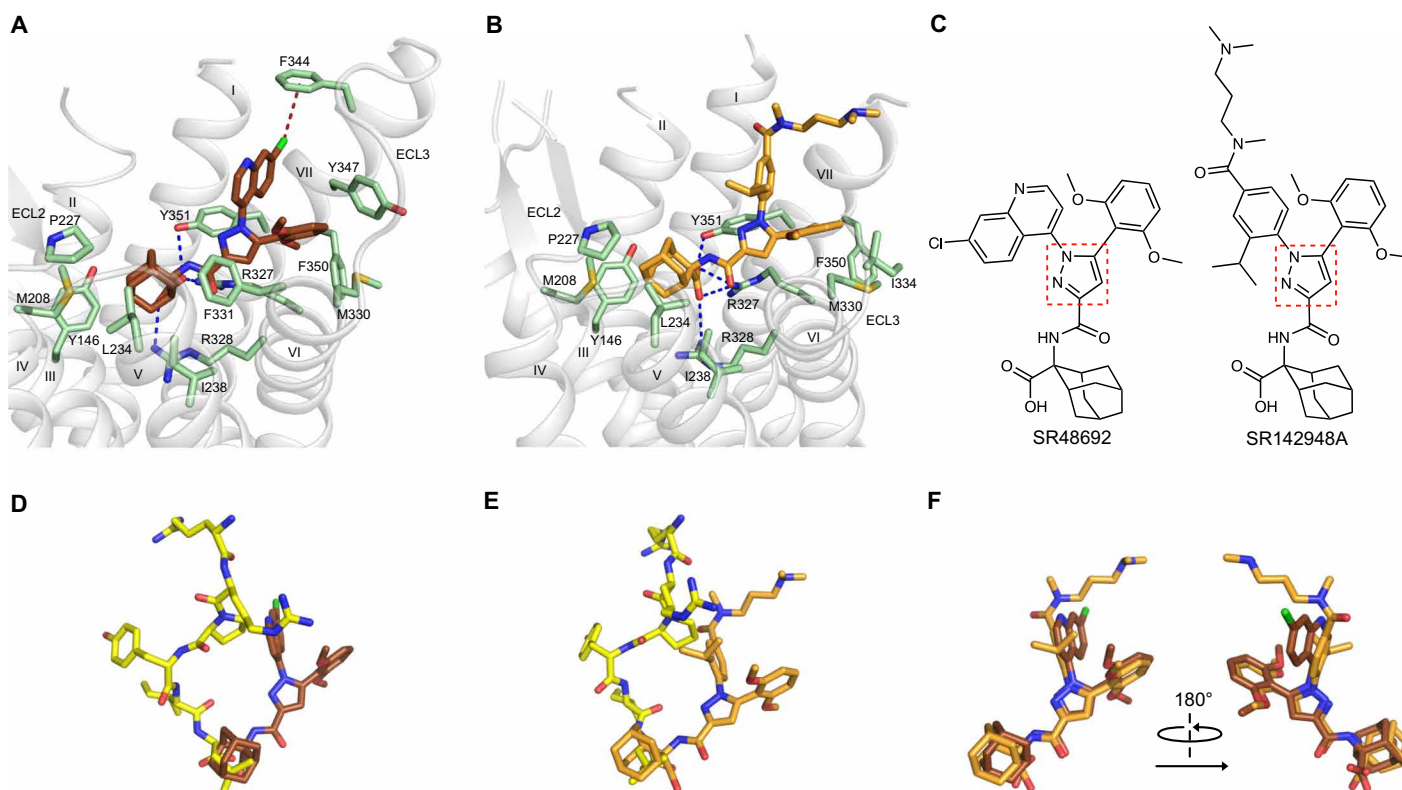


Fig. 4. Inverse agonist-binding pockets of rNTSR1 and superposition of binding modes. (A and B) Detailed interactions of (A) NTSR1-H4bm_X bound to SR48692 (IA) and (B) NTSR1-H4_X bound to SR142948A (IA), viewed from the extracellular side. The receptor backbone is depicted in cartoon representation and is colored in light gray. Ligands are shown as sticks, SR48692 is colored brown, and SR142948A is colored orange. Interacting receptor residues are shown as sticks in pale green. L234 is a mutation present in NTSR1-H4 and NTSR1-H4bm (V in wild-type rNTSR1). H-bonds and salt bridges are depicted by dashed blue lines and halogen- π interactions by dashed red lines. The DARPIn fusion has been omitted for clarity. In the SR142948A complex, the side chains of F331 and Y347, which may form hydrophobic contacts with the ligand, were not well resolved by their electron density and were therefore not modeled. The alkylamine chain of the latter ligand is likely directed toward the extracellular space but is not visible in the electron density, probably due to its conformational flexibility (fig. S5E) (20). (C) Chemical structures of SR48692 and SR142948A. The pyrazole core scaffold of each ligand is highlighted by a dashed red rectangle. (D to F) Comparison of the binding modes of (D) NTS₈₋₁₃ (FA) and SR48692 (IA), (E) NTS₈₋₁₃ (FA) and SR142948A (IA), and (F) SR48692 (IA) and SR142948A (IA), viewed from a similar perspective as in (A) and (B). FA, full agonist; IA, inverse agonist. NTS₈₋₁₃ is depicted in yellow. After superposition, the receptor has been omitted for clarity.

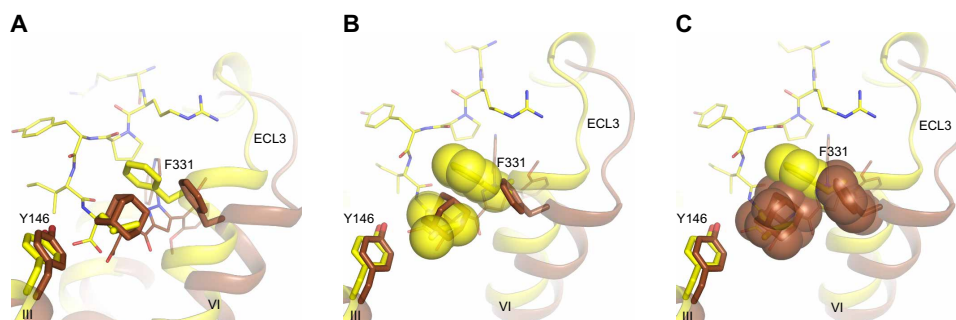


Fig. 5. Steric effects of the isobutyl and adamantyl groups of agonists and inverse agonists, respectively. (A to C) Superposition of the NTS₈₋₁₃ (FA) and SR48692 (IA) complexes solved in this study, showing (A) the tilting of TM6 at F331^{6,58} and (B) highlighting the space occupied by the isobutyl chain of Leu₁₃ and by F331^{6,58} as well as (C) the space occupied by the adamantyl moiety and by F331^{6,58}, viewed from the membrane plane. FA, full agonist; IA, inverse agonist. The receptor backbone is depicted in cartoon representation. The NTS₈₋₁₃ complex is colored in yellow, and the SR48692 complex is colored in brown. Side chains are shown as sticks and are colored as the corresponding backbone. The isobutyl chain of Leu₁₃ and the adamantyl moiety of SR48692 are shown as sticks and as van der Waals spheres, while the rest of the ligands are shown as thin sticks. F331^{6,58} is also shown as van der Waals spheres. TM4, ECL2, TM5, and TM7 have been omitted for clarity.

no contacts tethering to the ECL2 β hairpin at the opposite side of the extracellular portion (Fig. 4, A and B). Overall, these differences and their structural consequences probably explain the inability of SR48692 and SR142948A to activate NTSR1 and provide a rationale of how they may stabilize the inactive state.

ECL3 and TM7 interactions are crucial for agonist-induced NTSR1 activation

Although the presence of an L-Leu moiety is highly beneficial for agonist potency and efficacy (21, 22, 48), its presence is not sufficient to guarantee receptor activation (neither full nor partial), and the question thus arises of how other functional groups in agonist ligands modulate receptor activation. The structures obtained in this study now allow us to broadly address this question.

All three agonists bind near the receptor center (Fig. 3, A to C). Where they extend toward the extracellular space, they form contacts on one wall of the binding site with TM6, ECL3, and TM7, while at the opposite wall they are tethered to the ECL2 β hairpin and TM2, indicating that this anchoring pattern may be important for inducing the contraction of the extracellular receptor portion. While the role of the L-Leu moiety in receptor activation appears to be largely related to TM6 (discussed above), the other functional groups in agonistic ligands appear to modulate receptor activation via rearrangements of ECL3 and the extracellular tip of TM7 (Fig. 6, A to D). Site-directed mutagenesis studies identified a set of aromatic rNTSR1 residues belonging to these regions as important mediators of agonist potency [(49); Fig. 6E]. Mutagenesis of W339^{ECL3}, F344^{7,28}, Y347^{7,31}, H348^{7,32}, and Y349^{7,33} to Ala, or Phe in the case of Y347^{7,31}, caused a moderate drop in NTS₈₋₁₃ affinity; however, it also led to a substantially stronger reduction in potency at the G_q pathway [(49); Fig. 6E] and G_s pathway (49) (~100- and 1000-fold, respectively). Furthermore, it has been observed that these mutations shift the conformational equilibrium of the receptor toward a low-affinity agonist-binding state (49). Together, these findings suggest that the aforementioned residues not only are involved in agonist binding but also are essential for stabilization of a contracted binding site as required for high-potency G protein activation.

NTS₈₋₁₃ interacts with W339^{ECL3} and other residues in ECL3, and with F344^{7,28}, Y347^{7,31}, and H348^{7,32} in TM7 (Fig. 3A and table S5), stabilizing their arrangement toward the receptor center. In contrast, weak or no electron density is observed for W339^{ECL3}, F344^{7,28}, and

H348^{7,32} in the apo structure (fig. S6F), indicating higher flexibility within these regions due to the lack of stabilizing interactions that are seen in the NTS₈₋₁₃ complex. Furthermore, in the NTS₈₋₁₃ complex, the side chain of H348^{7,32} is oriented toward the receptor core, accompanied by an inward rotation of Y349^{7,33} and an inward movement of the extracellular tip of TM7 (Fig. 6A). In analogy to NTS₈₋₁₃, the full agonist SRI-9829 also interacts with W339^{ECL3}, F344^{7,28}, Y347^{7,31}, and H348^{7,32} (Fig. 3B and table S6), leading to a marked inward movement of ECL3 and the extracellular tip of TM7 (Fig. 6B). Of note, while NTS₈₋₁₃ establishes several polar interactions with these regions, SRI-9829 largely relies on van der Waals and aromatic contacts, with the indole and quinoline rings representing excellent hydrophobic platforms.

In strong contrast to the full agonists, the partial agonist RTI-3a forms fewer and weaker interactions with W339^{ECL3} and F344^{7,28} (Fig. 3C and table S7). Furthermore, the chloroquinoline ring partially covers the space occupied by the H348^{7,32} side chain in the NTS₈₋₁₃ and SRI-9829 complexes, apparently hindering the inward rotation of H348^{7,32} (Fig. 6C), with the location of the extracellular tip of TM7 being reminiscent of the apo structure. Structure-activity studies indicated that the chlorine substituent is essential for the agonistic properties of this ligand (21), which could be related to the halogen- π contacts formed with H348^{7,32}, nonetheless tethering this ligand to the tip of TM7.

The extent by which agonist binding can alter the orientation of the aforementioned residues is highlighted by comparison of the NTS₈₋₁₃ complex with the structure bound to the inverse agonist SR48692. In the latter structure, the side chains of F344^{7,28}, Y347^{7,31}, and H348^{7,32} are considerably further away from the receptor center than in the NTS₈₋₁₃ complex (by 6.2, 8.9, and 5.7 Å, respectively, as measured between ring centers) (Fig. 6D), and while weak or no electron density is observed for the side chains of W339^{ECL3} and Y349^{7,33} (fig. S12A), their backbone is more distant as well (by 6.7 and 3.5 Å, respectively). Furthermore, in the SR48692 complex, this cluster of aromatic residues is too distant or flexible to form a stable network of aromatic interactions, whereas such a network is established in the complexes with the full agonists (Fig. 6, A and B) and thus possibly contributes to stabilization of a contracted arrangement of the binding site. In the complex with the partial agonist, this network is partially severed by the outward orientation of H348^{7,32} (Fig. 6C), while it is completely absent in the apo structure,

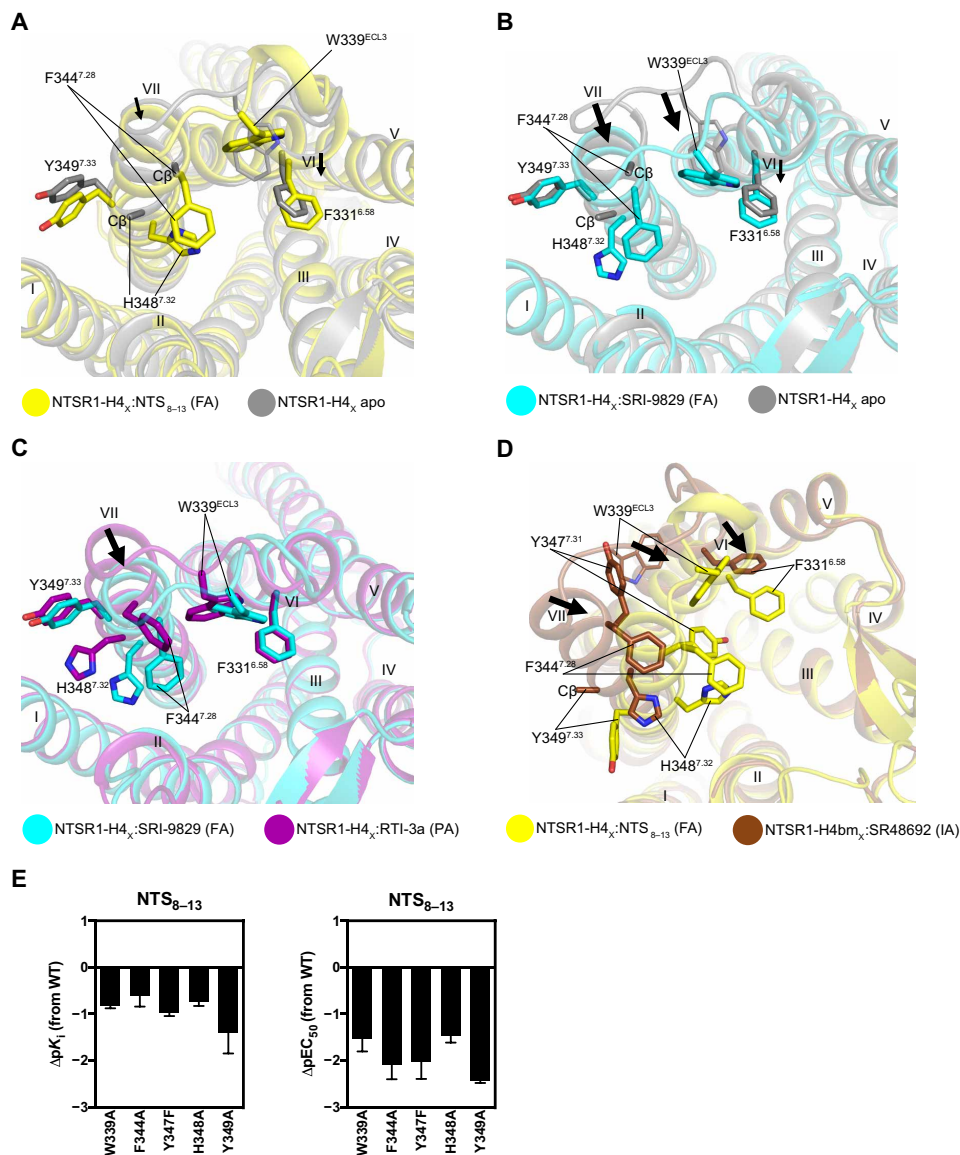


Fig. 6. Backbone and side-chain perturbations in the extracellular rNTSR1 portion induced by ligand binding. (A and B) Superposition of the apo structure with the complexes of (A) NTS₈₋₁₃ (FA) and (B) SRI-9829 (FA), viewed from the extracellular side. (C) Superposition of the SRI-9829 (FA) and RTI-3a (PA) complexes. (D) Superposition of the NTS₈₋₁₃ (FA) and SR48692 (IA) complexes. FA, full agonist; PA, partial agonist; IA, inverse agonist. Backbone and key residues are shown as cartoon and sticks, respectively, and are colored as indicated in the legend. In the apo structure and SR48692 complex, W339 is poorly visible in the electron density (figs. S6F and S12A) and is thus shown as transparent thin sticks. C β indicates that the side chain is not visible in the electron density. Backbone rearrangements between 1 and 3 Å are indicated by thin black arrows, and backbone rearrangements >3 Å are indicated by thick black arrows. The ligands, the receptor N terminus, and the DARPIn have been omitted for clarity. (E) Differences in NTS₈₋₁₃ affinity (pK_i) or potency at G_q signaling (pEC_{50}) for selected mutants relative to wild-type rNTSR1. pK_i values were derived from competition ligand-binding experiments (table S8), and pEC_{50} values were derived from concentration-response curves (table S9). Data are shown as means \pm SEM from 3 to 11 independent experiments performed in duplicate.

due to increased flexibility within these regions (Fig. 6A and fig. S6F). Overall, the interactions mediated by agonist ligands with ECL3 and TM7, as well as the resulting structural changes presented here, are likely crucial determinants of ligand-induced NTSR1 activation, in agreement with functional studies.

Interhelical polar network and hydrophobic core in NTSR1 activation

Having established structural details of how agonists cause a contraction of the extracellular portion of NTSR1 and how inverse agonists

act in the opposite direction and prevent it, the question arises of how these structural rearrangements are transmitted to the intracellular receptor portion. A network of polar interactions beneath the NTS₈₋₁₃ binding site has previously been proposed to link agonist binding with the hydrophobic receptor core (10, 11, 45). We therefore compared inverse agonist-bound NTSR1-H4bm χ with agonist-bound NTSR1-ELF (10), a minimal mutant with retained signaling properties. This comparison suggests that receptor activation may be favored by rotation of the D150^{3,33} side chain toward the central axis of the receptor (Fig. 7A). This rotation may go hand in hand

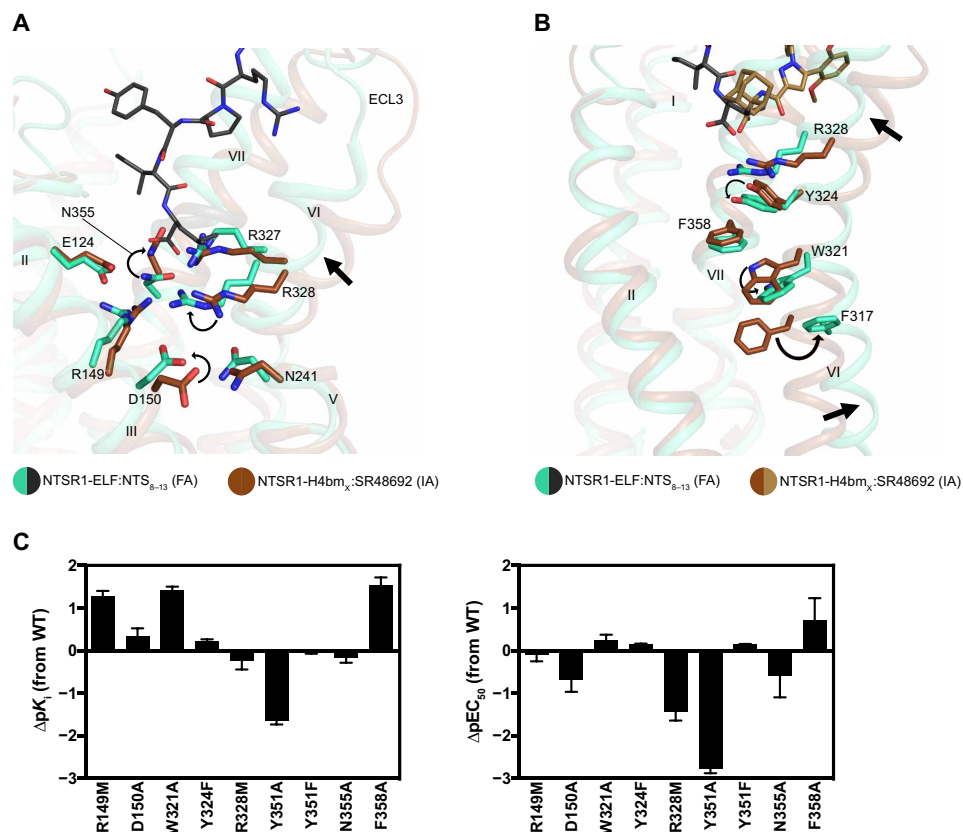


Fig. 7. Interhelical polar network and hydrophobic core residues. (A) Superposition of the interhelical polar network in agonist-bound NTSR1-ELF (PDB ID: 4XEE) (10) and inverse agonist-bound NTSR1-H4bm χ . FA, full agonist; IA, inverse agonist. TM4, ECL2, part of TM5, and fusion proteins have been omitted. (B) Hydrophobic core residues of the same structures as in (A). ECL1, TM3 to TM5, and fusion proteins have been omitted. Receptor residues are shown as sticks, and the ligands are shown as thin sticks. Backbone, residues, and ligands are colored as indicated in the legend. Relevant side-chain rearrangements are indicated by black curved arrows, whereas backbone rearrangements are indicated by black straight arrows. (C) Effect of single residues on agonist binding and receptor activation. Bars represent differences in calculated affinity (pK_i) or potency at G_q signaling (pEC₅₀) for each mutant relative to wild-type rNTSR1. pK_i values for NTS₈₋₁₃ were derived from competition ligand-binding experiments (table S8); pEC₅₀ values for NTS₈₋₁₃-induced IP1 generation were derived from concentration-response curves (table S9). Data are shown as means \pm SEM from three to five independent experiments performed in duplicate.

with the rotation of the guanidinium head group of R328^{6,55} toward the agonist's carboxylate, as captured in the structure of NTSR1-ELF (10). The rearrangement of the latter side chain may underlie the highly beneficial effect of a carboxylate group for ligand agonism (22), in addition to the anchoring function exerted through a salt bridge with R327^{6,54} (Fig. 3, A to C). Furthermore, the carboxylate group of the agonist appears to adopt a position closer to the central axis of the receptor compared to the homologous functional group of the inverse agonist (Fig. 7B). This positional difference might affect the rearrangements within the polar network and thus partially underlie the opposite biological functions of these carboxylate-carrying ligands. In the agonist-bound structure, R327^{6,54} interacts with N355^{7,39}, which is, in turn, linked to E124^{2,61}. In the inverse agonist-bound structure, we observed a substantial repositioning of N355^{7,39} (Fig. 7A), which appears to weaken the TM2-TM7 linkage.

To confirm our structural observations, we generated single mutants of D150^{3,33}, R328^{6,55}, and N355^{7,39} in wild-type rNTSR1 and probed the effect on agonist binding and G_q-mediated signaling (Fig. 7C). D150^{3,33}A, R328^{6,55}M, and N355^{7,39}A only slightly affect NTS₈₋₁₃ affinity; however, they result in a marked drop in agonist potency. This validates the hypothesis that the charges of D150^{3,33} and R328^{6,55}, as well as the N355^{7,39} side chain, are important for agonist-induced

receptor activation. Y351^{7,35} also takes part in the polar network via its hydroxyl group; however, this residue appears to exert its function mainly through its phenyl ring. This is evidenced by the retained NTS₈₋₁₃ affinity and potency upon mutation to Phe, but not to Ala (Fig. 7C), and could reflect an important role in the stabilization of R327^{6,54} through cation- π interactions.

R149^{3,32} is linked to TM2 via a salt bridge with E124^{2,61} and to TM7 via a cation- π interaction with F358^{7,42}. In a recent nuclear magnetic resonance (NMR) study on NTSR1-H4, it was shown that the mutation E124^{2,61}D, which weakens the interaction with R149^{3,32}, stabilizes the active state of the receptor (50). In agreement, the mutations R149^{3,32}M and F358^{7,42}A result in increased affinity for NTS₈₋₁₃ (Fig. 7C), indicating that these mutations likely shift the equilibrium toward active conformations, although only F358^{7,42}A also results in detectable constitutive activity (fig. S16) (19). Comparison of the active- and inactive-like structures does not reveal large rearrangements of R149^{3,32} and F358^{7,42} (Fig. 7, A and B); nonetheless, it is possible that transient weakening of these TM2-TM3 and TM3-TM7 contacts favors receptor activation. This could underlie, at least partially, the upward shift of TM3 corresponding to an active state at the intracellular side (1.5 Å at A157^{3,40} of the transmission switch motif). Upon agonist binding, R149^{3,32} may

thus sense the agonist's carboxylate and reorient its head group, weakening the interaction with E124^{2,61}.

F358^{7,42} is positioned between Y324^{6,51} and W321^{6,48} in a “hydrophobic cascade” (10), ending at F317^{6,44} of the transmission switch motif (Fig. 7B). W^{6,48} and F^{6,44} are regarded as crucial residues in class A GPCRs for the transmission of the agonist-induced activation trigger to the G protein-binding interface (51, 52). In other class A GPCRs, the role of W^{6,48} is related to the Na⁺-binding pocket and the associated H-bond network (53, 54). However, the role of W321^{6,48} in NTSR1 cannot be fully ascertained because of the absence of a functional Na⁺ pocket in the structures solved in this study. Nevertheless, we observe that the large shift of TM6 upon activation and the rotation of F317^{6,44} are not associated to large rearrangements of W321^{6,48}, although a slight tilting of the indole side chain of W321^{6,48} is observed in the inverse agonist-bound structure (Fig. 7B). This is interesting, as the relative orientation of W321^{6,48} to the membrane plane has previously been suggested to play a role in NTSR1 activation (10, 11). The tilting observed in the inverse agonist-bound structure could, in turn, be related to a slight upward shift of F358^{7,42} and Y324^{6,51}. The latter residue may thus link the polar network with the hydrophobic cascade, and our functional data indicate that it exerts its function mainly through its phenyl ring (Fig. 7C), which could suggest the involvement of cation- π interactions with R328^{6,55}. Unexpectedly, the mutation W321^{6,48}A does not substantially affect agonist-induced signaling (Fig. 7C) (11) or basal activity (fig. S16); however, it does lead to a substantial increase in NTS₈₋₁₃ affinity (Fig. 7C), which nonetheless supports the implication of W321^{6,48} in the modulation of NTSR1 conformational equilibrium (10, 11). Together, our structural and functional data thus suggest that, for receptor activation, a number of rather subtle conformational rearrangements are required beneath the binding pocket, most likely involving water molecules, and that subtle movements in the hydrophobic core critically modulate the network of interhelical interactions. Understanding the exact role played by water molecules will need further studies, as the resolution of the inverse agonist-bound inactive structures solved in this study does not allow to assess changes in the position of structured water molecules compared to the agonist-bound state.

DISCUSSION

NTSR1 recognizes the endogenous peptides NTS and neuromedin N. In light of the receptor's physiological relevance, a number of synthetic compounds with diverse biological effects have been developed; however, their exact binding modes and structural rationales of action have remained unclear, which precluded a more comprehensive understanding of the receptor activation and inactivation mechanisms. To elucidate the detailed structural determinants of agonism and inverse agonism at a peptidergic GPCR and to unravel the binding modes of synthetic NTSR1 lead compounds, we thus embarked in a major crystallographic effort and solved structures of rNTSR1 bound to full, partial, and inverse agonists, as well as in the apo state.

To achieve this, the new crystallization design exploiting the fusion to the DARPIn D12 chaperone (39–41) was crucial to make this study possible: The DARPIn provided strong crystal contacts, while the shared helix design (39) proved to be an ideal compromise between rigidity and malleability, adapting to different crystal packings. This design has thus the potential to enable structure determina-

tion of other challenging targets that have so far resisted to crystallization, perhaps also in complex with several ligands of various efficacies. As for traditional intracellular loop 3 (ICL3) fusions, potential structural effects related to a rigidly fused DARPIn crystallization chaperone will require a careful assessment on a case-by-case basis in future studies, in particular at the intracellular side and proximal to the fusion site on TM7. In our study, fusion of DARPIn D12 to TM7 via the reported shared helix design did not cause any relevant structural deviation in the 7TM bundle of NTS₈₋₁₃-bound NTSR1-H4 compared to the structure obtained without fusion (PDB ID: 4BWB) (9), nor did it affect the binding pocket or ligand affinities. Furthermore, our crystallized complexes, bound to the same ligands but exhibiting different crystal packings and DARPIn orientations, reveal that, although deviations proximal to the fusion site can occur, the conformations adopted by the receptor and the ligand-binding modes are identical or highly similar. Altogether, these findings validate this approach as a valuable tool for GPCR crystallography.

All structures presented in this study, including the agonist complexes, adopt a closed helical arrangement at the cytosolic side. This is a common outcome in the absence of a G protein, or a mimic thereof, which would stabilize a more open conformation. In addition, it has previously been proposed that a mutation present in NTSR1-H4, namely, R167^{3,50}L, may favor a closed conformation at the cytosolic side through a “hydrophobic lock” mechanism (9), and we found this mutation to be crucial for crystallization of the complexes presented in this study. The gain of knowledge for the agonist complexes is thus mostly concentrated to the extracellular portion, as the structures were obtained without a G protein. The inverse agonist complexes exhibit nonetheless a further closure at the cytosolic side, in particular of TM6. Thus, to gain insights into the mechanism of signal transmission from the binding site to the cytosolic side, we reverted four interfering mutations (generating NTSR1-H4bm_X) and compared the inverse agonist-bound inactive conformation (of NTSR1-H4bm_X) to previously published structures captured in the active or active-like state at the cytosolic side. Structural observations were subsequently evaluated in binding and functional assays in the context of wild-type rNTSR1.

The extracellular portion of our crystallized constructs appears to be conformationally more flexible, as we observed helical and side-chain rearrangements in the different ligand complexes and in the apo structure. At the extracellular side, the latter exhibits an intermediate conformation between the agonist complexes and the inverse agonist ones, yet it is more similar to the agonist-bound state, which might appear surprising. However, it should be considered that most GPCRs naturally sample different conformations in their apo form, and it is not straightforward to predict which one will correspond to an energy minimum in the well-diffracting crystals. Furthermore, it is possible that the presence of stabilizing mutations has contributed to shifting the equilibrium toward active-like conformations at the extracellular side, as suggested by the increased affinity for full agonists.

Nonetheless, in the inverse agonist-bound state, the structures solved in this study reveal a pronounced outward tilting of the extracellular ends of TM6, and especially TM7, and of ECL3. The inverse agonists largely share the same binding site as the agonists; however, they adopt a notably tilted binding mode, pointing toward (and almost partially intercalating between) TM6 and TM7. This corroborates the observation that peptide-binding GPCRs exhibit a broad spectrum of ligand-binding

modes (55), i.e., ligands can occupy a diverse space within the transmembrane bundle or extracellular vestibule. The bulky adamantyl moiety of the NTSR1 inverse agonists appears to play a crucial role in the opening of the extracellular receptor portion, which translates to a closure of the helical bundle at the intracellular side.

Of note, it remains a possibility that a ligand could bind and stabilize multiple receptor conformations besides the one captured crystallographically, as GPCRs are known to adopt various conformations within the different states (inactive, intermediate, and active) they sample. A future area of research should thus focus on this aspect; however, this may require the use of experimental and computational methods more suitable than crystallography to assess the dynamics of NTSR1 conformational equilibria.

The inactive state of wild-type NTSR1 is likely stabilized by Na⁺ ions, as observed for several other GPCRs (53). Unfortunately, no NTSR1 structure to date captured a functional Na⁺-binding pocket, which therefore needs to be addressed by future studies. Nevertheless, the structures solved in this study shed additional light on the polar network beneath the agonist-binding site and on the hydrophobic core residues that are involved in the transmission of the activation trigger to the intracellular side. Moreover, on the basis of the sequence conservation of many crucial residues discussed above, such as F^{6.44}, W^{6.48}, Y/F^{6.51}, R^{6.55}, F/Y^{6.58}, and F^{7.42}, it is likely that several other members of the ghrelin family share similar principles by which the activation trigger is transmitted within the hydrophobic core to elicit large-scale helical rearrangements. Our structural insights have thus the potential to improve the understanding of other physiologically important peptide-binding receptors.

As for NTSR1, none of the ghrelin family receptors has been clinically exploited to date (3, 4). However, after a lag phase of almost two decades, it appears that ligands targeting these receptors are close to provide proven therapeutic benefits (56–58). For example, recently, the radiopharmaceutical ¹⁷⁷Lu-3BP-227 (57) based on the NTSR1 ligand SR142948A showed promise for treatment of ductal pancreatic adenocarcinoma (58), one of the cancers with the highest mortality rates, and is expected to be evaluated in clinical trials to treat solid tumors.

Our structural findings also expand the understanding of how agonists induce a contraction of the binding site, which has broad implications. Noteworthy, the development of the novel nonpeptide full agonist SRI-9829 was key to elucidate structural determinants of NTSR1 activation, as it allowed us to compare receptor interactions with the chemically divergent full agonist NTS_{8–13}. The complex with SRI-9829 reveals that this nonpeptidic full agonist based on an indole core occupies a similar space in the pocket as the C-terminal tetrapeptide of NTS_{8–13} and mimics its contacts, leading to a similar contraction of the binding site as induced by NTS_{8–13}. However, the lack of a moiety forming additional interactions, as Arg₈ and Arg₉ do in NTS_{8–13}, probably explains the lower affinity and potency compared to the hexapeptide at wild-type rNTSR1, suggesting a possible direction for the design of highly potent small-molecule full agonists. In contrast to the full agonists, the complex with the partial agonist RTI-3a exhibits a slightly less contracted binding site, in particular at TM7, which probably translates into a less favored opening of the cytosolic side for interactions with the G protein, explaining its reduced efficacy.

Overall, it appears that potent NTSR1 full agonists require contacts reaching up to the extracellular tip of TM7 and ECL3. In this regard, the subtle difference between rat and human NTSR1 at position F/Y^{7.28} at the extracellular tip of TM7 needs to be carefully considered for ligand

design. Ligand-mediated interactions with TM7 may also be of particular relevance in light of the known role of TM7 in biased signaling (59).

In conclusion, this study presents the first structures of NTSR1 bound to small-molecule ligands, ranging from inverse to full agonists, as well as of the apo state, made possible by a new crystallization design. Thereby, we elucidated structural determinants of full, partial, and inverse agonism at a peptidergic receptor, deepening our mechanistic understanding of GPCRs and providing new templates for structure-based drug screening and design.

MATERIALS AND METHODS

Synthesis of SRI-9829

A step-by-step synthesis procedure of SRI-9829, as well as the corresponding NMR and mass spectrometry characterizations are reported in Supplementary Materials and Methods.

Generation of NTSR1-H4_x and NTSR1-H4bm_x constructs

The rNTSR1 mutant NTSR1-H4 had been obtained previously by directed evolution (table S1) (34). NTSR1-H4_x was obtained by introducing the following modifications: deletion of N-terminal residues M1–A49 and ICL3 residues E273–T290, and fusion of DARPIn D12 (39–41) to residue L371^{7.55} via the linker sequence AEDLVEDWE (creating a shared helix), as depicted in fig. S2, thereby deleting rNTSR1 residues V372–Y424. The software suite Rosetta was used to optimize the sequence of the shared helix and of possibly contacting residues. DARPIn D12 was thus modified in its N-terminal region by deletion of residues S1 and D2 and by introduction of four point mutations, namely L3K, G4A, K5R, and A13K. Furthermore, the last two C-terminal D12 residues L157 and N158 were both mutated to alanine. Of note, the C-terminal region of the crystallized fusion construct, which includes a short linker sequence followed by a cleaved 3C protease site (see below), turned out to be partially α -helical and established crystal contacts. The receptor construct NTSR1-H4bm_x is identical to NTSR1-H4_x, with the exception that the receptor harbors the back-mutations D124^{2.61}E, E150^{3.33}D, V358^{7.42}F, and A362^{7.46}S, restoring the wild-type residues. For expression in *Escherichia coli*, the genes encoding the receptor constructs were cloned into a previously described pBR322-derived vector (35). Briefly, this resulted in an expression construct consisting of an N-terminal maltose-binding protein (MBP), followed by a His₆-tag, a human rhinovirus (HRV) 3C protease cleavage site (LEVLFQGP), a short linker (GS), the receptor itself fused to DARPIn D12, a short linker (TRE), a second HRV 3C protease cleavage site, followed by thioredoxin A (TrxA), and a C-terminal His₁₀-tag.

Expression and solubilization of NTSR1-H4_x and NTSR1-H4bm_x

NTSR1-H4_x and NTSR1-H4bm_x were expressed in *E. coli* BL21 cells bearing a deletion of the *fhuA2* gene to confer phage T1 resistance (New England Biolabs). A starter culture of cells harboring the expression plasmid was grown overnight at 37°C in 2×YT medium containing 1% (w/v) glucose and ampicillin (100 µg/ml). One liter of expression cultures consisting of 2×YT, 0.2% (w/v) glucose, and ampicillin (100 µg/ml) was inoculated with the starter culture to an OD₆₀₀ (optical density at 600 nm) of ~0.05 and grown at 37°C to an OD₆₀₀ of ~0.5, followed by induction with 1 mM isopropyl- β -D-thiogalactopyranoside (IPTG) and cultivation for 18 hours at 28°C.

Cells were harvested by centrifugation at 5000g for 20 min at 4°C, typically yielding ~7 g of pellet per 1 liter of culture. The cell pellet was resuspended with Resuspension Buffer [100 mM Hepes (pH 8.0), 30% (v/v) glycerol, and 400 mM NaCl] at 4°C, frozen in liquid nitrogen, and stored at –80°C.

All the following steps were carried out at 4°C. Typically, 60 ml of frozen resuspended cells (corresponding to 20 g of pellet) was thawed and incubated with lysozyme (2 mg/ml) (Sigma-Aldrich), 5 mM MgCl₂, and deoxyribonuclease (DNase) I (0.05 mg/ml) (Roche) for 1 hour while stirring. For NTSR1-H4bm_x, but not NTSR1-H4_x, either NTS₈₋₁₃ (AnaSpec) or SR48692 (Tocris) was added to a final concentration of 15 μM. Subsequently, receptors were solubilized by incubation with 2% (w/v) *n*-dodecyl-β-D-maltopyranoside (DDM; Anatrace) and 0.2% (w/v) cholesteryl hemisuccinate (CHS; Sigma-Aldrich) for 1 hour while stirring followed by sonication for 30 min using a Sonifier 250 (Branson) at a duty cycle of 30% and output of 5.

Purification of NTSR1-H4_x and NTSR1-H4bm_x for LCP crystallization

All the following steps were carried out at 4°C. The lysate containing detergent-solubilized receptor was adjusted with imidazole (pH 8.0) to a final concentration of 20 mM and centrifuged at 20,000g for 30 min. For NTSR1-H4bm_x, but not NTSR1-H4_x, all subsequent buffers were supplemented with 10 μM of either NTS₈₋₁₃ or SR48692 (final concentration). The supernatant was batch-incubated overnight with 20 ml of TALON Superflow resin (GE Healthcare) equilibrated with Wash Buffer I [25 mM Hepes (pH 8.0), 10% (v/v) glycerol, 600 mM NaCl, 0.1% (w/v) DDM, 5 mM MgCl₂, 2 mM 2-mercaptoethanol (2-ME), and 20 mM imidazole (pH 8.0)]. Subsequently, the resin was washed with 10 column volumes (CVs) of Wash Buffer I followed by 5 CVs of Wash Buffer II [25 mM Hepes (pH 8.0), 10% (v/v) glycerol, 150 mM NaCl, 0.1% (w/v) DDM, 2 mM 2-ME, and 20 mM imidazole (pH 8.0)]. Protein elution was carried out with 3 CVs of Elution Buffer [25 mM Hepes (pH 7.0), 10% (v/v) glycerol, 150 mM NaCl, 0.1% (w/v) DDM, 2 mM 2-ME, and 250 mM imidazole (pH 8.0)]. The eluted protein was concentrated in two 100-kDa molecular weight cutoff Vivaspin 20 concentrators (Sartorius) to 2.5 ml each and subsequently desalted using two PD MiniTrap G-25 columns (GE Healthcare) equilibrated with G-25 Buffer [10 mM Hepes (pH 7.0), 10% (v/v) glycerol, 0.05% (w/v) DDM, and 2 mM dithiothreitol (DTT)]. The protein was incubated for 3 hours with HRV 3C protease (produced in-house) to cleave off the fusion proteins MBP and TrxA. The mixture was loaded onto 2.5 ml of SP Sepharose cation exchange chromatography resin (GE Healthcare) equilibrated with G-25 Buffer. The resin was washed with 5 CVs of SP Wash Buffer I [10 mM Hepes (pH 7.7), 10% (v/v) glycerol, 35 mM NaCl, 0.025% (w/v) DDM, and 2 mM DTT] and with 5 CVs of SP Wash Buffer II [10 mM Hepes (pH 7.0), 10% (v/v) glycerol, 0.025% (w/v) DDM, 0.005% (w/v) CHS, and 2 mM DTT] to remove the fusion proteins MBP and TrxA. Protein elution was carried out stepwise using 12 ml of SP Elution Buffer [10 mM Hepes (pH 7.0), 10% (v/v) glycerol, 500 mM NaCl, 0.015% (w/v) DDM, 0.003% (w/v) CHS, and 2 mM DTT]. Fractions containing more than 0.6 mg/ml protein were combined and adjusted with SP Elution Buffer to 0.6 to 0.7 mg/ml in a typical final volume of 2.4 ml. Protein concentrations were determined by absorbance at 280 nm using a NanoDrop 2000 spectrophotometer (Thermo Fisher Scientific). Purified apo NTSR1-H4_x was incubated overnight either without addition of any ligand or

with 300 μM of either SRI-9829, RTI-3a (Tocris; commercial name, TC NTR1 17), SR48692 (Axon MedChem and Tocris), SR142948A (Axon MedChem), or NTS₈₋₁₃ (AnaSpec and GenScript). Purified NTS₈₋₁₃- or SR48692-bound NTSR1-H4bm_x was incubated overnight with 300 μM of the respective ligand. Subsequently, the protein sample was concentrated with a 100-kDa molecular weight cutoff Vivaspin 2 concentrator (Sartorius) to ~60 mg/ml, resulting in a typical final volume of 25 μl.

Purification of NTSR1-H4_x for vapor diffusion crystallization

All the following steps were carried out at 4°C. NTSR1-H4_x was purified from the lysate containing detergent-solubilized receptor via a pD-NT ligand affinity column followed by detergent exchange to nonyl-β-D-glucopyranoside (NG), 3C protease cleavage, and SP Sepharose cation exchange chromatography essentially as previously described (9, 35), with the exception that the final buffer exchange was carried out on a PD MiniTrap G-25 column (GE Healthcare) instead of by preparative gel filtration on a Superdex 200 10/300 GL column. The bound ligand consists of NTS₈₋₁₃ with an additional four residues at its N terminus (GPGG), as it is cleaved off from the ligand affinity column.

Crystallization in LCP

Apo and ligand-bound NTSR1-H4_x, as well as ligand-bound NTSR1-H4bm_x, were reconstituted in LCP by mixing concentrated protein (~60 mg/ml) with molten monoolein (Sigma-Aldrich) supplemented with 10% (w/w) cholesterol (Sigma-Aldrich) at a protein-to-lipid ratio of 20:32 (v/v) using the two-syringe method (100-μl syringes; Hamilton). Crystallization trials were carried out at 20°C in 96-well glass sandwich plates (SWISSCI) with a 120-μm spacer. A Crystal Gryphon LCP crystallization robot (Art Robbins Instruments) was used to dispense 40-nl boli and to cover them with 800 nl of precipitant solution. The plates were immediately sealed with a cover glass and incubated at 20°C in Rock Imager 1000 (Formulatrix). All crystals obtained in this study were of rather small size, typically not exceeding ~15 to 30 μm in any dimension. NTSR1-H4_x, in complex with the ligands cocrystallized in this study, yielded crystals in a wide range of conditions in initial crystallization screens. Initial conditions were fine-screened and yielded optimized crystals used for data collection. Optimized crystallization conditions are summarized in table S12. Crystals were harvested by picking the entire bolus at room temperature with 25-μm MicroMesh (MiTeGen) and flash-frozen in liquid nitrogen without adding further cryoprotectant.

Crystallization by vapor diffusion

Concentrated NTS₈₋₁₃-bound NTSR1-H4_x (~10 mg/ml) was adjusted to 0.6% (w/v) (final concentration) *n*-nonyl-β-D-glucoside (NG). Sitting drop crystallization trials were carried out at 4°C in 96-well Intelli-Plate 96-3 LVR plates (Art Robbins Instruments) containing 75 μl of precipitant solution in each reservoir. A Crystal Gryphon crystallization robot (Art Robbins Instruments) was used to dispense 0.5-μl drops of protein solution and to add 0.5 μl of precipitant solution. The plates were immediately sealed with a plastic foil and incubated at 4°C in a Rock Imager 1000 (Formulatrix). Optimized crystals of NTS₈₋₁₃-bound NTSR1-H4_x used for data collection grew in a precipitant solution consisting of 50 mM glycine (pH 9.4), 1 M NaCl, and 8.3% (w/v) PEG4000 (polyethylene glycol, molecular weight 4000). Crystals were harvested using 0.2- to 0.4-mm loops

and cryoprotected by incubation for ~10 s in a solution containing 50 mM glycine (pH 9.4), 1 M NaCl, 0.3% (w/v) NG, 15% (v/v) PEG600, and 15% (v/v) glycerol. Cryoprotected crystals were flash-frozen in liquid nitrogen.

Data collection and structure determination

Collection of x-ray diffraction data was carried out at the X06SA (PXI) beamline at the Swiss Light Source of the Paul Scherrer Institute (Villigen, Switzerland). Mounted samples were kept in a cryostream at 100 K, and diffraction data were collected using a wavelength of 1 Å and an EIGER 16M detector. Crystals embedded in LCP were located by diffraction using a grid scan protocol with a nonattenuated beam and an exposure time of 0.04 s. Data collection parameters were adjusted to optimize the signal-to-noise ratio. For crystals of NTSR1-H4_X in complex with SRI-9829 and RTI-3a, diffraction data were recorded using the SSX suite (60). Partial datasets (minisets) were typically recorded using a 15 μm × 15 μm or 20 μm × 30 μm nonattenuated beam, an exposure time of 0.1 s, an oscillation angle of 0.2°, and an angular wedge of 10° to 20°. For crystals of NTSR1-H4bm_X in complex with SR48692 and NTS₈₋₁₃, partial datasets were recorded using a 15 μm × 15 μm beam attenuated to 50%, an exposure time of 0.05 s, an oscillation angle of 0.2°, and an angular wedge of 20°. For crystals of NTSR1-H4_X bound to NTS₈₋₁₃ obtained by vapor diffusion crystallization, diffraction data were collected with a 30 μm × 30 μm attenuated beam, an exposure time of 0.05 s, a total angular range of 180°, and an oscillation angle of 0.1°. Datasets were obtained either from one or two large crystals (NTSR1-H4_X bound to NTS₈₋₁₃, SR48692, SR142948A, and for the apo form) or from a set of approximately 20 smaller LCP crystals that had similar cell parameters (NTSR1-H4_X bound to SRI-9829 and RTI-3a, and NTSR1-H4bm_X bound to NTS₈₋₁₃ and SR48692). The data were indexed and integrated with XDS, while scaling was performed with AIMLESS within the CCP4 package. As all datasets of the several different crystal forms suffered from substantial anisotropic diffraction, data were anisotropy-corrected and merged using the STARANISO server (61) from Global Phasing Ltd. Starting with the best data, the structure of the NTSR1-H4_X:NTS₈₋₁₃ complex was determined by molecular replacement using PHASER, with the GPCR domain of 4XEE (10) as the search model. The top solution was then refined in multiple rounds of model building with COOT and refinement with BUSTER and REFMAC. Validation during the course of refinement was performed using MolProbity within the PHENIX package. The coordinates of chain A of the NTSR1-H4_X:NTS₈₋₁₃ complex were thereafter used to determine the structures of the apo form and the other complexes using the same approach. Statistics for data collection and refinement of all structures can be found in tables S3 and S4.

Structural analysis

Receptors were structurally aligned using the command “align” in PyMOL and the 7TM bundle as template. To determine the RMSD_{Cα} value in the extracellular receptor half between NTS₈₋₁₃-bound NTSR1-H4_X and NTSR1-ELF (PDB ID: 4XEE) (10), only the residues in the extracellular half were aligned. Residues located above the conserved W321^{6,48} of the CWxP motif were considered to belong to the extracellular half, i.e., residues 51 to 72, 118 to 154, 197 to 245, and 321 to 358, resulting in 146 Cα positions. Unless otherwise stated, distances were generally measured between Cα atoms for backbone rearrangements, between ring centers for aromatic residues, and between polar atoms for polar interactions. Rearrange-

ments of the extracellular tips of TM6 and TM7 were determined between corresponding Cα atoms of residue 333^{6,60} for TM6 and residue 342^{7,26} for TM7. The receptor center is defined as the central axis of the 7TM bundle perpendicular to the membrane plane. Orthosteric ligand-binding cavity volumes were calculated with the program POVME 2.0 (62). As the cocrystallized ligands exhibited distinct extensions toward the extracellular receptor opening, an identical inclusion region obtained from the combined ligand dimensions from all structures was used to define the cavity boundaries.

Mammalian cell culture

Human embryonic kidney (HEK) 293T/17 cells and COS-7 cells (American Type Culture Collection) were cultivated in Dulbecco's modified medium (Sigma-Aldrich) supplemented with penicillin (100 U/ml), streptomycin (100 μg/ml) (Sigma-Aldrich), and 10% (v/v) fetal calf serum (BioConcept). Cells were maintained at 37°C in a humidified atmosphere of 5% CO₂ and 95% air. Transient transfections were performed with TransIT-293 (Mirus Bio) or Lipofectamine LTX (Thermo Fisher Scientific) for HEK293T/17 and COS-7 cells, respectively, according to the manufacturer's instructions.

Ligand-binding assays

Ligand-binding experiments were performed on whole cells or on cell membranes obtained from transiently transfected HEK293T/17 using a homogeneous time-resolved fluorescence (HTRF) binding assay. All receptor variants were cloned into a mammalian expression vector containing an N-terminal SNAP-tag (Cisbio), and point mutations were introduced by site-directed mutagenesis. The constructs NTSR1-H4_X and NTSR1-H4_X^{ΔD12} are identical to the receptor construct used for crystallization, including a cleaved 3C protease site (GP) followed by a short linker (GS) at the N terminus and a short linker (TRE) followed by the cleaved 3C protease site (LEVLFQ) at the C terminus. In the construct NTSR1-H4_X^{ΔD12}, DARPin D12 was replaced by the wild-type rNTSR1 sequence V372–G390. HEK293T/17 cells were transiently transfected with receptor constructs and were seeded at 20,000 cells per well in poly-L-lysine-coated 384-well plates (Greiner) for whole-cell binding assays or at 5 × 10⁶ cells in 10-cm petri dishes for membrane preparation. Forty-eight hours after transfection, cells were labeled with 50 nM SNAP-Lumi4-Tb (Cisbio) in assay buffer [20 mM Hepes (pH 7.5), 100 mM NaCl, 3 mM MgCl₂, and 0.2% (w/v) nonfat milk] for 1.5 hours at 37°C. Thereafter, cells were washed four times with assay buffer and used directly for whole-cell ligand-binding experiments, or crude cell membrane extracts were prepared as described before (63). Cells or 0.2- to 1-μg membranes per well were then incubated for 4 hours at room temperature in assay buffer containing fluorescently labeled peptide HL488-NTS₈₋₁₃ (NTS₈₋₁₃ labeled with HiLyte Fluor 488 at the N terminus) (Eurogentec). For competition binding, 0.5 to 100 nM HL488-NTS₈₋₁₃ tracer peptide and concentration ranges of unlabeled competitor ligands were used. Fluorescence intensities were measured on an Infinite M1000 fluorescence plate reader (Tecan) with an excitation wavelength of 340 nm and emission wavelengths of 620 and 520 nm for Tb³⁺ and fluorophore HiLyte Fluor 488, respectively. The ratio of FRET (fluorescence resonance energy transfer) donor and acceptor fluorescence intensities (F520/F620 nm) was calculated. Total binding was obtained in the absence of competitor, and nonspecific binding was determined in the presence of 100 μM unlabeled NTS₈₋₁₃. Data were normalized to the specific binding for each individual experiment and were analyzed

by global fitting to a one-site heterologous competition equation with the GraphPad Prism software (version 6.07). To obtain K_i values, data were corrected for fluorescent ligand occupancy of each mutant with the Cheng-Prusoff equation (64).

Signaling assays

All signaling assays were performed with receptor constructs harboring the full-length C terminus. Ligand-induced IP1 (a metabolite of IP3) accumulation was measured in transiently transfected HEK293T/17 cells, as described before (65). Basal receptor activity was measured in COS-7 cells transiently transfected with $G\alpha_q$ and the respective receptor construct. Twenty-four hours after transfection, cells were washed with phosphate-buffered saline (PBS), detached with trypsin-EDTA, and resuspended in assay buffer [10 mM Hepes (pH 7.4), 1 mM $CaCl_2$, 0.5 mM $MgCl_2$, 4.2 mM KCl, 146 mM NaCl, 50 mM LiCl, 5.5 mM glucose, and 0.2% (w/v) bovine serum albumin (BSA)]. Cells were seeded at 20,000 cells per well in white 384-well plates (Greiner) and incubated for 2 hours at 37°C with a concentration range of ligands diluted in assay buffer. For basal receptor activity, cells were resuspended in assay buffer devoid of LiCl and ligand. Basal IP1 accumulation was then initiated by adding 50 mM LiCl for the indicated time intervals. IP1 accumulation was determined using the HTRF IP-One Kit (Cisbio) according to the manufacturer's protocol. Fluorescence intensities were measured on an Infinite M1000 fluorescence plate reader (Tecan). To generate concentration-response curves, data were analyzed by a three-parameter logistic equation in GraphPad Prism software (version 6.07). For time-dependent basal IP1 generation, data were normalized to IP1 concentrations obtained from stimulation of the respective receptor construct with 10 μ M NTS₈₋₁₃ for 120 min and analyzed by linear regression.

SUPPLEMENTARY MATERIALS

Supplementary material for this article is available at <http://advances.sciencemag.org/cgi/content/full/7/5/eabe5504/DC1>

[View/request a protocol for this paper from Bio-protocol.](#)

REFERENCES AND NOTES

- J. P. Vincent, J. Mazella, P. Kitabgi, Neurotensin and neurotensin receptors. *Trends Pharmacol. Sci.* **20**, 302–309 (1999).
- B. Holst, N. D. Holliday, A. Bach, C. E. Elling, H. M. Cox, T. W. Schwartz, Common structural basis for constitutive activity of the ghrelin receptor family. *J. Biol. Chem.* **279**, 53806–53817 (2004).
- K. Sriram, P. A. Insel, G protein-coupled receptors as targets for approved drugs: How many targets and how many drugs? *Mol. Pharmacol.* **93**, 251–258 (2018).
- D. S. Wishart, Y. D. Feunang, A. C. Guo, E. J. Lo, A. Marcu, J. R. Grant, T. Sajed, D. Johnson, C. Li, Z. Sayeeda, N. Assempour, I. Iynkkaran, Y. Liu, A. Maciejewski, N. Gale, A. Wilson, L. Chin, R. Cummings, D. Le, A. Pon, C. Knox, M. Wilson, DrugBank 5.0: A major update to the DrugBank database for 2018. *Nucleic Acids Res.* **46**, D1074–D1082 (2018).
- J. A. Henry, D. C. Horwell, K. G. Meecham, D. C. Rees, A structure-affinity study of the amino acid side-chains in neurotensin: N and C terminal deletions and Ala-scan. *Bioorg. Med. Chem. Lett.* **3**, 949–952 (1993).
- C. Granier, J. van Rietschoten, P. Kitabgi, C. Poustis, P. Freychet, Synthesis and characterization of neurotensin analogues for structure/activity relationship studies. Acetyl-neurotensin-(8–13) is the shortest analogue with full binding and pharmacological activities. *Eur. J. Biochem.* **124**, 117–124 (1982).
- É. Besserer-Offroy, R. L. Brouillette, S. Lavenus, U. Froehlich, A. Brumwell, A. Murza, J.-M. Longpré, É. Marsault, M. Grandbois, P. Sarret, R. Leduc, The signaling signature of the neurotensin type 1 receptor with endogenous ligands. *Eur. J. Pharmacol.* **805**, 1–13 (2017).
- J. F. White, N. Noinaj, Y. Shibata, J. Love, B. Kloss, F. Xu, J. Gvozdenovic-Jeremic, P. Shah, J. Shiloach, C. G. Tate, R. Grishammer, Structure of the agonist-bound neurotensin receptor. *Nature* **490**, 508–513 (2012).
- P. Eglhoff, M. Hillenbrand, C. Klenk, A. Batyuk, P. Heine, S. Balada, K. M. Schlinkmann, D. J. Scott, M. Schütz, A. Plückthun, Structure of signaling-competent neurotensin receptor 1 obtained by directed evolution in *Escherichia coli*. *Proc. Natl. Acad. Sci. U.S.A.* **111**, E655–E662 (2014).
- B. E. Krumm, J. F. White, P. Shah, R. Grishammer, Structural prerequisites for G-protein activation by the neurotensin receptor. *Nat. Commun.* **6**, 7895 (2015).
- B. E. Krumm, S. Lee, S. Bhattacharya, I. Botos, C. F. White, H. Du, N. Vaidehi, R. Grishammer, Structure and dynamics of a constitutively active neurotensin receptor. *Sci. Rep.* **6**, 38564 (2016).
- H. E. Kato, Y. Zhang, H. Hu, C.-M. Suomivuori, F. M. N. Kadji, J. Aoki, K. Krishna Kumar, R. Fonseca, D. Hilger, W. Huang, N. R. Latorraca, A. Inoue, R. O. Dror, B. K. Kobilka, G. Skiniotis, Conformational transitions of a neurotensin receptor 1- $G_{\beta\gamma}$ complex. *Nature* **572**, 80–85 (2019).
- D. Gully, M. Canton, R. Boiegrain, F. Jeanjean, J. C. Molimard, M. Poncelet, C. Gueudet, M. Heaulme, R. Leyris, A. Brouard, Biochemical and pharmacological profile of a potent and selective nonpeptide antagonist of the neurotensin receptor. *Proc. Natl. Acad. Sci. U.S.A.* **90**, 65–69 (1993).
- D. Gully, B. Labeeuw, R. Boiegrain, F. Oury-Donat, A. Bachy, M. Poncelet, R. Steinberg, M. F. Suaud-Chagny, V. Santucci, N. Vita, F. Pecceu, C. Labbé-Jullié, P. Kitabgi, P. Soubrié, G. Le Fur, J. P. Maffrand, Biochemical and pharmacological activities of SR 142948A, a new potent neurotensin receptor antagonist. *J. Pharmacol. Exp. Ther.* **280**, 802–812 (1997).
- R. E. Carraway, A. M. Plona, Involvement of neurotensin in cancer growth: Evidence, mechanisms and development of diagnostic tools. *Peptides* **27**, 2445–2460 (2006).
- Z. Wu, D. Martinez-Fong, J. Trédaniel, P. Forgez, Neurotensin and its high affinity receptor 1 as a potential pharmacological target in cancer therapy. *Front. Endocrinol. (Lausanne)* **3**, 184 (2013).
- Q. Ouyang, J. Zhou, W. Yang, H. Cui, M. Xu, L. Yi, Oncogenic role of neurotensin and neurotensin receptors in various cancers. *Clin. Exp. Pharmacol. Physiol.* **44**, 841–846 (2017).
- J. Liu, M. Agopianz, J. Poupon, Z. R. Wu, P.-A. Just, B. Borghese, E. Ségal-Bendirdjian, G. Gauchotte, A. Gompel, P. Forgez, Neurotensin receptor 1 antagonist SR48692 improves response to carboplatin by enhancing apoptosis and inhibiting drug efflux in ovarian cancer. *Clin. Cancer Res.* **23**, 6516–6528 (2017).
- S. Barroso, F. Richard, D. Nicolas-Ethève, P. Kitabgi, C. Labbé-Jullié, Constitutive activation of the neurotensin receptor 1 by mutation of Phe(358) in helix seven. *Br. J. Pharmacol.* **135**, 997–1002 (2002).
- R. C. Kling, M. Plomer, C. Lang, A. Banerjee, H. Hübner, P. Gmeiner, Development of covalent ligand-receptor pairs to study the binding properties of nonpeptidic neurotensin receptor 1 antagonists. *ACS Chem. Biol.* **11**, 869–875 (2016).
- J. B. Thomas, H. Navarro, K. R. Warner, B. Gilmour, The identification of nonpeptide neurotensin receptor partial agonists from the potent antagonist SR48692 using a calcium mobilization assay. *Bioorg. Med. Chem. Lett.* **19**, 1438–1441 (2009).
- P. Di Fruscia, Y. He, M. Koenig, S. Tabrizifard, A. Nieto, P. H. McDonald, T. M. Kamenecka, The discovery of indole full agonists of the neurotensin receptor 1 (NTSR1). *Bioorg. Med. Chem. Lett.* **24**, 3974–3978 (2014).
- F. St-Gelais, C. Jomphe, L.-E. Trudeau, The role of neurotensin in central nervous system pathophysiology: What is the evidence? *J. Psychiatry Neurosci.* **31**, 229–245 (2006).
- M. Boules, Z. Li, K. Smith, P. Fredrickson, E. Richelson, Diverse roles of neurotensin agonists in the central nervous system. *Front. Endocrinol.* **4**, 36 (2013).
- W. C. Mustain, P. G. Rychahou, B. M. Evers, The role of neurotensin in physiologic and pathologic processes. *Curr. Opin. Endocrinol. Diabetes Obes.* **18**, 75–82 (2011).
- O. Osadchii, A. Woodiwiss, G. Norton, *Neuropeptide Research Trends Ch. 1* (Nova Science Publishers, 2007), pp. 13–63.
- K. Kalafatakis, K. Triantafyllou, Contribution of neurotensin in the immune and neuroendocrine modulation of normal and abnormal enteric function. *Regul. Pept.* **170**, 7–17 (2011).
- J. Li, J. Song, Y. Y. Zaytseva, Y. Liu, P. Rychahou, K. Jiang, M. E. Starr, J. T. Kim, J. W. Harris, F. B. Yiannikouris, W. S. Katz, P. M. Nilsson, M. Orho-Melander, J. Chen, H. Zhu, T. Fahrenholz, R. M. Higashi, T. Gao, A. J. Morris, L. A. Cassis, T. W.-M. Fan, H. L. Weiss, P. R. Dobner, O. Melander, J. Jia, B. M. Evers, An obligatory role for neurotensin in high-fat-diet-induced obesity. *Nature* **533**, 411–415 (2016).
- O. E. Osadchii, Emerging role of neurotensin in regulation of the cardiovascular system. *Eur. J. Pharmacol.* **762**, 184–192 (2015).
- A. M. Piliponosky, C.-C. Chen, T. Nishimura, M. Metz, E. J. Rios, P. R. Dobner, E. Wada, K. Wada, S. Zacharias, U. M. Mohanasundaram, J. D. Faix, M. Abrink, G. Pejler, R. G. Pearl, M. Tsai, S. J. Galli, Neurotensin increases mortality and mast cells reduce neurotensin levels in a mouse model of sepsis. *Nat. Med.* **14**, 392–398 (2008).
- B. M. Evers, Neurotensin and growth of normal and neoplastic tissues. *Peptides* **27**, 2424–2433 (2006).
- C. Labbé-Jullié, S. Barroso, D. Nicolas-Ethève, J. L. Reversat, J. M. Botto, J. Mazella, J. M. Bernassau, P. Kitabgi, Mutagenesis and modeling of the neurotensin receptor NTR1. Identification of residues that are critical for binding SR 48692, a nonpeptide neurotensin antagonist. *J. Biol. Chem.* **273**, 16351–16357 (1998).

33. M. Lückmann, B. Holst, T. W. Schwartz, T. M. Frimurer, In silico investigation of the neurotensin receptor 1 binding site: Overlapping binding modes for small molecule antagonists and the endogenous peptide agonist. *Mol. Inform.* **35**, 19–24 (2016).
34. D. J. Scott, L. Kummer, P. Egloff, R. A. D. Bathgate, A. Plückthun, Improving the apo-state detergent stability of NTS₁ with CHESS for pharmacological and structural studies. *Biochim. Biophys. Acta* **1838**, 2817–2824 (2014).
35. P. Egloff, M. Deluigi, P. Heine, S. Balada, A. Plückthun, A cleavable ligand column for the rapid isolation of large quantities of homogeneous and functional neurotensin receptor 1 variants from *E. coli*. *Protein Expr. Purif.* **108**, 106–114 (2015).
36. P. Heine, G. Witt, A. Gilardi, P. Gribbon, L. Kummer, A. Plückthun, High-throughput fluorescence polarization assay to identify ligands using purified G protein-coupled receptor. *SLAS Discov.* **24**, 915–927 (2019).
37. A. Ranganathan, P. Heine, A. Rudling, A. Plückthun, L. Kummer, J. Carlsson, Ligand discovery for a peptide-binding GPCR by structure-based screening of fragment- and lead-like chemical libraries. *ACS Chem. Biol.* **12**, 735–745 (2017).
38. E. Chun, A. A. Thompson, W. Liu, C. B. Roth, M. T. Griffith, V. Katritch, J. Kunen, F. Xu, V. Cherezov, M. A. Hanson, R. C. Stevens, Fusion partner toolchest for the stabilization and crystallization of G protein-coupled receptors. *Structure* **20**, 967–976 (2012).
39. Y. Wu, A. Batyuk, A. Honegger, F. Brandl, P. R. E. Mittl, A. Plückthun, Rigidly connected multispecific artificial binders with adjustable geometries. *Sci. Rep.* **7**, 11217 (2017).
40. P. Ernst, A. Honegger, F. van der Valk, C. Ewald, P. R. E. Mittl, A. Plückthun, Rigid fusions of designed helical repeat binding proteins efficiently protect a binding surface from crystal contacts. *Sci. Rep.* **9**, 16162 (2019).
41. P. R. E. Mittl, P. Ernst, A. Plückthun, Chaperone-assisted structure elucidation with DARPins. *Curr. Opin. Struct. Biol.* **60**, 93–100 (2020).
42. F. Bumbak, A. C. Keen, N. J. Gunn, P. R. Gooley, R. A. D. Bathgate, D. J. Scott, Optimization and ¹³CH₃ methionine labeling of a signaling competent neurotensin receptor 1 variant for NMR studies. *Biochim. Biophys. Acta* **1860**, 1372–1383 (2018).
43. T. Warne, P. C. Edwards, A. S. Doré, A. G. W. Leslie, C. G. Tate, Molecular basis for high-affinity agonist binding in GPCRs. *Science* **364**, 775–778 (2019).
44. T. Che, S. Majumdar, S. A. Zaidi, J. D. McCorvy, S. Wang, P. D. Mosier, R. Uprety, E. Vardy, B. E. Krumm, G. W. Han, M.-Y. Lee, E. Pardon, J. Steyaert, X.-P. Huang, R. T. Strachan, A. R. Tribo, G. W. Pasternak, F. I. Carroll, R. C. Stevens, V. Cherezov, V. Katritch, D. Wacker, B. L. Roth, Structure of the nanobody-stabilized active state of the kappa opioid receptor. *Cell* **172**, 55–67.e15 (2018).
45. S. Nagarajan, N. J. Alkayed, S. Kaul, A. P. Barnes, Effect of thermostable mutations on the neurotensin receptor 1 (NTSR1) activation state. *J. Biomol. Struct. Dyn.* **38**, 340–353 (2020).
46. P. Kitabgi, C. Poustis, C. Granier, J. van Rietschoten, J. Rivier, J.-L. Morgat, P. Freychet, Neurotensin binding to extraneural and neural receptors: Comparison with biological activity and structure—Activity-relationships. *Mol. Pharmacol.* **18**, 11–19 (1980).
47. F. Bumbak, T. Thomas, B. J. Noonan-Williams, T. M. Vaid, F. Yan, A. R. Whitehead, S. Bruell, M. Kocan, X. Tan, M. A. Johnson, R. A. D. Bathgate, D. K. Chalmers, P. R. Gooley, D. J. Scott, Conformational changes in tyrosine 11 of neurotensin are required to activate the neurotensin receptor 1. *ACS Pharmacol. Transl. Sci.* **3**, 690–705 (2020).
48. P. M. Herschberger, M. P. Hedrick, S. Peddibhotla, A. Mangravita-Novo, P. Gosalia, Y. Li, W. Gray, M. Vicchiarelli, L. H. Smith, T. D. Y. Chung, J. B. Thomas, M. G. Caron, A. B. Pinkerton, L. S. Barak, G. P. Roth, Imidazole-derived agonists for the neurotensin 1 receptor. *Bioorg. Med. Chem. Lett.* **24**, 262–267 (2014).
49. F. Richard, S. Barroso, D. Nicolas-Ethève, P. Kitabgi, C. Labbé-Jullié, Impaired G protein coupling of the neurotensin receptor 1 by mutations in extracellular loop 3. *Eur. J. Pharmacol.* **433**, 63–71 (2001).
50. I. Goba, D. Goricanec, D. Schum, M. Hillenbrand, A. Plückthun, F. Hagn, Probing the conformation states of neurotensin receptor 1 variants by NMR site-directed methyl labeling. *ChemBiochem*, in press (2020).
51. V. Katritch, V. Cherezov, R. C. Stevens, Structure-function of the G protein-coupled receptor superfamily. *Annu. Rev. Pharmacol. Toxicol.* **53**, 531–556 (2013).
52. W. I. Weis, B. K. Kobilka, The molecular basis of G protein-coupled receptor activation. *Annu. Rev. Biochem.* **87**, 897–919 (2018).
53. V. Katritch, G. Fenalti, E. E. Abola, B. L. Roth, V. Cherezov, R. C. Stevens, Allosteric sodium in class A GPCR signaling. *Trends Biochem. Sci.* **39**, 233–244 (2014).
54. W. Shihoya, T. Izume, A. Inoue, K. Yamashita, F. M. N. Kadji, K. Hirata, J. Aoki, T. Nishizawa, O. Nureki, Crystal structures of human ET_B receptor provide mechanistic insight into receptor activation and partial activation. *Nat. Commun.* **9**, 4711 (2018).
55. F. Wu, G. Song, C. de Graaf, R. C. Stevens, Structure and function of peptide-binding G protein-coupled receptors. *J. Mol. Biol.* **429**, 2726–2745 (2017).
56. S. M. Advani, P. G. Advani, H. M. VonVille, S. H. Jafri, Pharmacological management of cachexia in adult cancer patients: A systematic review of clinical trials. *BMC Cancer* **18**, 1174 (2018).
57. J. Schulz, M. Rohracker, M. Stiebler, J. Goldschmidt, F. Stöber, M. Noriega, A. Pethe, M. Lukas, F. Osterkamp, U. Reineke, A. Höhne, C. Smerling, H. Amthauer, Proof of therapeutic efficacy of a ¹⁷⁷Lu-labeled neurotensin receptor 1 antagonist in a colon carcinoma xenograft model. *J. Nucl. Med.* **58**, 936–941 (2017).
58. R. P. Baum, A. Singh, C. Schuchardt, H. R. Kulkarni, I. Klette, S. Wiessalla, F. Osterkamp, U. Reineke, C. Smerling, ¹⁷⁷Lu-3BP-227 for neurotensin receptor 1-targeted therapy of metastatic pancreatic adenocarcinoma: First clinical results. *J. Nucl. Med.* **59**, 809–814 (2018).
59. N. R. Latorraca, A. J. Venkatakrishnan, R. O. Dror, GPCR dynamics: Structures in motion. *Chem. Rev.* **117**, 139–155 (2017).
60. S. Basu, J. W. Kaminski, E. Panepucci, C. Y. Huang, R. Warshamane, M. Wang, J. A. Wojdyla, Automated data collection and real-time data analysis suite for serial synchrotron crystallography. *J. Synchrotron Radiat.* **26**, 244–252 (2019).
61. I. J. Tickle, C. Flensburg, P. Keller, W. Paciorek, A. Sharff, C. Vornrhein, G. Bricogne, STARANISO (2018); <http://staraniso.globalphasing.org>.
62. J. D. Durrant, L. Votapka, J. Sørensen, R. E. Amaro, POVME 2.0: An enhanced tool for determining pocket shape and volume characteristics. *J. Chem. Theory Comput.* **10**, 5047–5056 (2014).
63. C. Klenk, T. Vetter, A. Zürn, J.-P. Vildaraga, P. A. Friedman, B. Wang, M. J. Lohse, Formation of a ternary complex among NHERF1, β -arrestin, and parathyroid hormone receptor. *J. Biol. Chem.* **285**, 30355–30362 (2010).
64. Y.-C. Cheng, W. H. Prusoff, Relationship between the inhibition constant (K_i) and the concentration of inhibitor which causes 50 per cent inhibition (I_{50}) of an enzymatic reaction. *Biochem. Pharmacol.* **22**, 3099–3108 (1973).
65. J. Ehrenmann, J. Schöppe, C. Klenk, M. Rappas, L. Kummer, A. S. Doré, A. Plückthun, High-resolution crystal structure of parathyroid hormone 1 receptor in complex with a peptide agonist. *Nat. Struct. Mol. Biol.* **25**, 1086–1092 (2018).
66. S. Huber, F. Casagrande, M. N. Hug, L. S. Wang, P. Heine, L. Kummer, A. Plückthun, M. Hennig, SPR-based fragment screening with neurotensin receptor 1 generates novel small molecule ligands. *PLoS ONE* **12**, e0175842 (2017).
67. C. R. Martinez, B. L. Iverson, Rethinking the term "pi-stacking". *Chem. Sci.* **3**, 2191–2201 (2012).
68. H. C. Jubb, A. P. Higuero, B. Ochoa-Montaño, W. R. Pitt, D. B. Ascher, T. L. Blundell, Arpeggio: A web server for calculating and visualising interatomic interactions in protein structures. *J. Mol. Biol.* **429**, 365–371 (2017).
69. Y. N. Imai, Y. Inoue, I. Nakanishi, K. Kitaura, Cl- π interactions in protein-ligand complexes. *Protein Sci.* **17**, 1129–1137 (2008).

Acknowledgments: We thank B. Blattmann and C. Müller-Simmen of the Protein Crystallization Center at the University of Zurich for support during crystallization and the staff of the X06SA beamline at the Paul Scherrer Institute for support during x-ray data collection. We also thank M. Hilge for support during x-ray data collection, data processing, and refinement of the crystal structures. We thank S. J. Novick for collecting high-resolution mass spectrometry data for the synthesis and characterization of SRI-9829. **Funding:** This work was supported by Schweizerische Nationalfonds grant 31003A_182334 (to A.P.).

Author contributions: A.H. designed the NTSR1-DARPin fusion. M.D., A.K. and L.Me. cloned, expressed, purified, and crystallized the NTSR1-DARPin fusion and harvested crystals. M.D. established expression and purification protocols with support from P.H. and P.Eg. S.V. supported expression and purification. M.D., A.K., and L.Me. collected x-ray diffraction data. M.D. supervised A.K., L.Me., and S.V. in the aforementioned tasks and organized and planned the experiments. P.R.E.M. and P.Er. contributed to x-ray data processing and refinement in the initial phase of this project. M.D. analyzed and interpreted structural data with support from C.K. and A.K. C.K., S.A.E., and L.Mo. cloned receptor mutants and performed ligand-binding and signaling experiments, and C.K. analyzed the data and organized and planned the experiments. T.M.K. and Y.H. designed and synthesized SRI-9829. Project management was carried out by M.D. and A.P. with support from C.K. The manuscript was prepared by M.D., A.K., C.K., and A.P. with inputs from all authors. All authors contributed to the final editing and approval of the manuscript. **Competing interests:** The authors declare that they have no competing interests. **Data and materials availability:** Coordinates and structure factors have been deposited in the worldwide PDB under the following accession codes: 6YVR (NTSR1-H4_x:NTS₈₋₁₃), 6Z8N (NTSR1-H4_x:SRI-9829), 6ZA8 (NTSR1-H4_x:RTI-3a), 6ZIN (NTSR1-H4_x:SR48692), 6Z4Q (NTSR1-H4_x:SR142948A), 6Z66 (apo NTSR1-H4_x), 6Z4V (NTSR1-H4bm_x:NTS₈₋₁₃), and 6Z4S (NTSR1-H4bm_x:SR48692). All data needed to evaluate the conclusions in the paper are present in the paper and/or the Supplementary Materials. Additional data related to this paper may be requested from the authors.

Submitted 29 August 2020

Accepted 9 December 2020

Published 27 January 2021

10.1126/sciadv.abe5504

Citation: M. Deluigi, A. Klipp, C. Klenk, L. Merklinger, S. A. Eberle, L. Morstein, P. Heine, P. R. E. Mittl, P. Ernst, T. M. Kamenecka, Y. He, S. Vacca, P. Egloff, A. Honegger, A. Plückthun, Complexes of the neurotensin receptor 1 with small-molecule ligands reveal structural determinants of full, partial, and inverse agonism. *Sci. Adv.* **7**, eabe5504 (2021).

Complexes of the neurotensin receptor 1 with small-molecule ligands reveal structural determinants of full, partial, and inverse agonism

Mattia Deluigi, Alexander Klipp, Christoph Klenk, Lisa Merklinger, Stefanie A. Eberle, Lena Morstein, Philipp Heine, Peer R. E. Mittl, Patrick Ernst, Theodore M. Kamenecka, Yuanjun He, Santiago Vacca, Pascal Egloff, Annemarie Honegger and Andreas Plückthun

Sci Adv 7 (5), eabe5504.
DOI: 10.1126/sciadv.abe5504

ARTICLE TOOLS

<http://advances.sciencemag.org/content/7/5/eabe5504>

SUPPLEMENTARY MATERIALS

<http://advances.sciencemag.org/content/suppl/2021/01/25/7.5.eabe5504.DC1>

REFERENCES

This article cites 66 articles, 12 of which you can access for free
<http://advances.sciencemag.org/content/7/5/eabe5504#BIBL>

PERMISSIONS

<http://www.sciencemag.org/help/reprints-and-permissions>

Use of this article is subject to the [Terms of Service](#)

Science Advances (ISSN 2375-2548) is published by the American Association for the Advancement of Science, 1200 New York Avenue NW, Washington, DC 20005. The title *Science Advances* is a registered trademark of AAAS.

Copyright © 2021 The Authors, some rights reserved; exclusive licensee American Association for the Advancement of Science. No claim to original U.S. Government Works. Distributed under a Creative Commons Attribution NonCommercial License 4.0 (CC BY-NC).